A Transit-Timing Variation Study of the Extrasolar Planet TrES-3
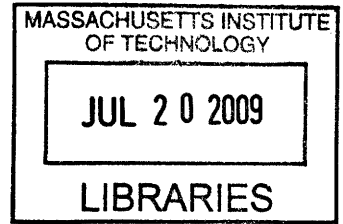
by

Matthew Lockhart

Submitted to the Department of Earth, Atmospheric, and Planetary Sciences
in partial fulfillment of the requirements for the degree of

Master of Science in Planetary Science

at the

MASSACHUSETTS INSTITUTE OF TECHNOLOGY

June 2009

Author ...
....
Department of Earth, Atmospheric, and Planetary Sciences
29 May 2009

Certified by
....
James L. Elliot
Professor
Department of Earth, Atmospheric, and Planetary Sciences
Thesis Supervisor

Accepted by ..
....
Maria T. Zuber
E. A. Griswold Professor of Geophysics
Head, Department of Earth, Atmospheric, and Planetary Sciences

A Transit-Timing Variation Study of the Extrasolar Planet TrES-3

by

Matthew Lockhart

Submitted to the Department of Earth, Atmospheric, and Planetary Sciences
on 29 May 2009, in partial fulfillment of the
requirements for the degree of
Master of Science in Planetary Science

Abstract

Portable Occultation Eclipse and Transit System (POETS) detectors [7] mounted on the Wallace Astrophysical Observatory (WAO) 0.8m and NASA Infrared Telescope Facility (IRTF) 3m telescopes are used to observe five stellar transit events of the extrasolar planet TrES-3 [5]. Model light curves are fit to the five data sets and transit midtimes are determined. Midtimes obtained in this study, along with midtimes reported by Sozzetti et al. (2008) [8], are compared to the ephemeris of the planet. The transit timing variation (TTV) of each midtime is calculated. Based on these data the presence of a third body in the TrES-3 system cannot be determined. Mass and period of a hypothetical perturbing body are calculated for several illustrative cases.

Thesis Supervisor: James L. Elliot
Title: Professor
Department of Earth, Atmospheric, and Planetary Sciences

Acknowledgments

I would like to thank: Mariana Baca, for making up for many of my shortcomings and tolerating the rest; Dr. Joe Bondaryk, for encouraging me to enter graduate school; Prof. Jim Elliot, for giving me an opportunity to do so; Elisabeth Adams, for a great deal of help at every stage of this project; Dr. Amanda Gulbis, for an instrument on Mauna Kea and couch space in Cape Town; and my parents, Forrest and Sandi Lockhart.

This research has made use of NASA's Astrophysics Data System Bibliographic Services.

Contents

List of Figures

List of Tables

Chapter 1

Introduction

An *extrasolar planet* is a planet known to orbit a star other than the Sun. If the orbital plane of such a planet is oriented such that an observer near the Sun views it nearly edge-on, it is possible for the planet to appear to cross the disk of its host star at some point in its orbit. This crossing, known as a *transit,* briefly blocks some of the observable starlight. A plot of the observed magnitude of the star as a function of time is known as a *light curve.* The depth and shape of the light curve of a transit event can be used to infer some of the properties of the planet and its orbit.

TrES-3 is a 1.9 M_{Jup} planet orbiting the 0.9 $M_{\odot}$ star GSC 03089-00929 (V magnitude 12.4, J2000.0 coordinates RA 17 52 07.03, Dec +37 32 46.1). It transits the star every 1.3 days, causing a roughly 2.5 percent decrease in observed flux [5].

TrES-3 was selected for study for several reasons. It is visible from the northern hemisphere. It is bright enough to be observed using modest telescopes and short (such that off-axis guiding is not necessary) exposure times. Photometric comparison stars of similar magnitude can be found nearby, yet no sources of significant magnitude are close enough to blend with it. A number of transit events were scheduled to be visible during the summer of 2008 when the majority of the data collection was to occur.

Observations were made in red light using Thorlabs 700nm longpass (see figure B-46) and Schüler / Astrodon Imaging Rs filters. This was done for two reasons. First, airglow is weak in this band, decreasing background light. Second, it was believed

that the effects of stellar limb darkening would be less significant in this band than in shorter-wavelength light, simplifying the analysis of recorded light curves.

Five TrES-3 transit events were observed successfully. The data sets were then calibrated. Differential aperture photometry was performed to generate a light curve for each event. Model light curves were then fit to the observed light curves in order to determine transit midtimes and other parameters. The resulting transit midtimes were then compared to the planet's published ephemeris.

Chapter 2

Instrumentation

2.1 Overview

The five transit events used in this research were recorded using Portable Occultation, Eclipse, and Transit System (POETS) detectors [7]. One detector was mounted to the 0.6-meter reflecting telescope at Wallace Astrophysical Observatory (WAO) in Westford, Massachusetts. A second detector was mounted to the 3.0-meter reflecting telescope at the NASA Infrared Telescope Facility (IRTF) on Mauna Kea in Hawaii.

A comparison of the two observatories used can be found in table A.1.

2.2 POETS

POETS detectors are manufactured by Andor Technology under the model name Ixon DV887. Each detector contains a 512-by-512-pixel frame-transfer CCD manufactured by E2V Technologies under the model name L3Vision. Reads of the CCD can be triggered by the detector itself when precise timing is not critical or by an outside timing source when precise timing is critical. During transit observations (in which precise timing is critical) reads of the CCD are triggered by a GPS receiver connected to the camera via a coaxial cable. The observer configures the GPS to produce trigger pulses at a specified start time and at specified intervals. The observer configures the camera to wait for external trigger signals and to allow a specified number of reads

to occur. The resulting set of images is stored as a FITS data cube.

The quantum efficiency of the POETS detector is shown in figure B-48.

2.3 WAO

2.3.1 Wavelength Band

The first of the transits observed from WAO was observed through a Thorlabs 700nm longpass filter (see figure B-46). On that night this filter was at WAO in order to undergo testing prior to its shipment to IRTF for use with the POETS detector there. The remaining two transits observed from WAO were observed through a Schüler / Astrodon Imaging Rs (red) filter (see figure B-47).

2.3.2 Pixel Scale and Field Size

Using a POETS frame from 20080921 at WAO and a distance measurement (between TrES-3 and a companion star) from Aladin [3], the POETS-WAO pixel scale was determined to be 0.36 arcseconds per pixel. This corresponds to a field width of about 3' 1". Figure B-2 is a sample image of the TrES-3 field recorded at WAO.

2.4 IRTF

2.4.1 Optics and Wavelength Band

The POETS detector at IRTF does not have its own dedicated instrument port. Instead, it is mounted to an auxiliary port of the SpeX instrument [6], an infrared spectrograph and imager.

A dichroic mirror within the SpeX instrument is used to split incoming light into two beams. Light with wavelength longward of 900nm is passed to Guidedog, one of the two detectors within the SpeX instrument. Light with wavelength shortward of 900nm is directed toward an auxiliary port on its way to the POETS detector. This light then passes through an optical adaptor package (designed to allow the POETS

detector to remain in the focal plane in spite of its position "downstream" of SpeX) and a Thorlabs 700nm longpass filter before striking the POETS detector. As a result the POETS detector observes in the 700nm-900nm wavelength band.

Images were recorded at IRTF using both the POETS and Guidedog detectors. The images recorded using the Guidedog detector were found to be noisy and were not used in this analysis.

2.4.2   Pixel Scale and Field Size

Using a POETS frame from 20080823 at IRTF and a distance measurement (between TrES-3 and a companion star) from Aladin, the POETS-IRTF pixel scale was determined to be 0.12 arcseconds per pixel. This corresponds to a field width of about 1' 1". Figure B-3 is a sample image of the TrES-3 field recorded at IRTF.

Chapter 3

Observations

3.1 Overview

The five nights of observations are summarized in table A.2.

3.2 WAO Guiding Difficulties

Two phenomena required manual repointing of the telescope during observations.

On all three observing nights (and up to several times per night) the field of view of the detector was observed to move abruptly relative to the sky. These jumps varied in size, but were sometimes large enough to move TrES-3 or the comparison star out of the field of view or uncomfortably close to its edge. In such cases the telescope was immediately manually repointed. The cause of the jumps was not determined with certainty. It was hypothesized that either the primary or the secondary mirror was insecurely mounted, changing its orientation slightly as hour angle, temperature, or other conditions changed. The time required for pointing jumps to occur was not determined precisely, though the star trails left on the detector during jumps were sufficiently faint that the jumps appeared to require only a small fraction of a typical 60-second or 120-second integration. Figure B-5 is a sample image showing the effect of a pointing jump. Images which were being exposed when jumps occurred were badly smeared and unusable for photometry.

The field of view of the detector also drifted slowly relative to the sky due to imperfections in the tracking provided by the telescope mount. This drift was predictable and was usually corrected with manual repointings performed between image cubes.

Manual repointing during the recording of image cubes was only performed when necessary, as images containing repointings (like images containing jumps) are badly smeared and unusable for photometry. Figure B-4 is a sample image showing the effect of a manual repointing.

Chapter 4

Calibration

4.1 Overview

Bias subtraction and flat-fielding were performed on all science images using IRAF. Images were archived once after bias-subtraction and again after flat-fielding. Access to these two datasets allowed the effectiveness of the flat-fielding to be determined. Details of the flat-fielding of the five nights of data are provided in table A.3.

4.2 Difficulties

The 20080823 and 20080827 data sets were initially flat-fielded using dome flats recorded on those nights. The results were unsatisfactory. These two data sets were ultimately flat-fielded using sky flats recorded on 20080907 in conjunction with the observation of a transit of CoRoT-Exo-2b. The flat-fielding did not work as well as had been hoped. The flat-fielded images were still used, however, as they yielded better light curves than the images which were only bias-subtracted.

The bias-subtracted images recorded at IRTF were strongly vignetted, the sky background appearing roughly three times as bright in the center of the frame as in the dimmest corner. This would have been acceptable (though the loss of photons would still have been unfortunate) if it had been possible to properly flat-field the images. Even after flat-fielding, however, background counts varied by nearly a factor

of two from the dimmest region of the field to the brightest. The photometry (see section 5) performed on those data sets suffered as a result.

It is not clear why the vignetting occurred. In December 2008 a diagonal mirror, suspected of being undersized, was replaced with a larger one by IRTF staff. The vignetting problem persisted. A light leak was discovered and corrected in May 2009. As of May 2009 the possibility of insufficient baffling admitting (inconsistent) off-axis light was under investigation.

Chapter 5

Photometry

5.1 Overview

Photometry involves determining how much light was received from an object in a particular length of time. Every pixel in a CCD image represents some number of detector counts recorded during the exposure of the image. The amount of light received from a particular object during an exposure can be determined by summing up the counts of the pixels occupied by the image of the object. *Aperture photometry* involves summing up the counts of all pixels within a particular region surrounding the image of the object. *Box photometry* is a straightforward form of aperture photometry involving a rectangular aperture centered on the image of the object. The same procedure is performed on an equally-sized box of pixels in a region of the image that contains sky background light but no actual sources. Subtracting the total number of counts in this region from the total number of counts in the object's region yields the number of counts generated by the object alone.

Another step must be performed. The varying transparency of the atmosphere, along with a number of other factors, causes the number of counts received per unit time from a particular source to vary significantly with time even if the source itself is constant. This can be calibrated out very effectively through *differential photometry*. During observation, care is taken to keep not only the object of interest, but another object (known as a *comparison* object) which is of comparable magnitude and which is

known to be intrinsically stable, inside the detector field. It is assumed that light from the two objects undergoes similar attenuation as it travels through the atmosphere and telescope optics. Box photometry is performed on both objects. The ratio of the total counts generated by the object of interest and the total counts generated by the comparison object is the reduced data point for that image. This process is then repeated for each image in a data set to form a light curve.

A star located 93 arcsec east-southeast (and generating roughly one-half the flux) of TrES-3 was used as a comparison star in the photometry performed on the WAO data sets. A star located 43.5 arcsec southwest (and generating roughly one-fifth the flux) of TrES-3 was used as a comparison star in the photometry performed on the IRTF data sets. The three stars can be seen in figure B-1.

Photometry was performed in Mathematica using a notebook (Mathematica script) written by Elisabeth Adams [1].

5.2 Procedure

A particular data set is selected and a list of aperture sizes entered. The initial positions of the target star, the comparison star, and a patch of blank sky are entered. If these positions do not move quickly from frame to frame, the notebook has the ability to follow the target star and keep the apertures roughly centered on it. Since the relative positions of the three locations are kept fixed, moving the target star moves all three positions (it is assumed that the objects will translate across the frame but not rotate within it). Large changes in target star position between frames, such as those caused by pointing jumps, can cause the notebook to lose the target star. A list of the filenames and frame numbers in which these jumps occur, along with new initial target star positions to be used in each case, is generated by hand and incorporated into the notebook.

A first round of data selection is then performed. The filenames and frame numbers of frames which are known to be unusable (either by visual inspection of the images or based on entries in the observing log) are entered. These frames are not

used for photometry. Aperture photometry is then performed on the target star and comparison star, using each aperture, for each of the remaining frames. These data are saved before being processed further.

A second round of data selection is then performed. A light curve is generated from the raw data (the specific aperture used is not very important here) and plotted. This raw light curve will often contain a few data points with values well above or below the surrounding noise. These points result from processes which briefly affect the brightness of the target and comparison stars differently, defeating the self-calibrating nature of differential photometry. Possible culprits are the passage of thin clouds or jet condensation trails through the field of view (at an altitude of ten kilometers one arcminute corresponds to a length of about three meters, so it is believable that a condensation trail might affect target and comparison stars separated by that amount differently) and the collision of high-speed particles with the detector near the image of one of the stars. Data points which are clearly aberrant (regardless of the specific cause), or which are above or below certain specified values, are singled out and formed into a list. The light curve is then replotted without those points. This process is repeated if necessary.

Light curves, stripped of the rejected points, are plotted for all apertures. A range of points which are all clearly baseline points (that is, which all occur outside the transit event) is recorded by hand in the notebook. The standard deviation of these points is calculated for each aperture. The aperture with the lowest standard deviation during baseline is considered the best aperture for that data set.

The best aperture size is recorded by hand in the notebook. The light curve generated using that aperture is then exported to disk both as a table of tab-separated values and as an image.

5.3   Output

Table A.4 lists the best aperture size for each night of data as well as the figure numbers of the resulting light curves and the figure numbers of plots of other interesting

27

quantities. The interesting quantities plotted (as a function of time) include: raw target-star counts, raw comparison-star counts, the diameter and x and y positions of the target star on the detector, and the airmass of the target field. These plots can be used to visualize changes in seeing, transparency, and guiding stability that occurred during a given night and to correlate those events with aberrant photometric data points and with changes in photometric precision.

Chapter 6

Fitting

6.1 Overview

A light curve by itself is of limited usefulness. To extract from the light curve the properties of the objects that produced it, a model light curve is generated (using a method detailed in appendix C) and its parameters are varied until the model light curve matches the observed light curve acceptably well. The parameters which resulted in the matching model light curve are interpreted as measurements of the actual system. The residuals (the amounts by which the data disagree with the model) are used to determine the uncertainties of these measurements. This process is known as *fitting*.

6.2 Parameters

The shape of a transit light curve is a function of several parameters. Section 6.2.1 defines these parameters and describes their effects on light curve shape. Figure B-21 provides a model transit light curve illustrating this shape.

6.2.1 Definitions

Duration

The *duration* of the transit is the elapsed time between *first contact* (when the disk of the planet first begins to overlap the disk of the star) and *fourth contact* (when the disk of the planet ceases overlapping the disk of the star). This affects the overall width of the light curve.

Radius Ratio

The *radius ratio* is the ratio of the planetary radius to the stellar radius. This parameter is dimensionless. Radius ratio strongly affects the depth of the light curve.

Impact Parameter

The *impact parameter* expresses the proximity, at closest approach, of the centers of the planet and star. This parameter is also dimensionless. A value of zero corresponds to the planet and star being concentric at the midtime of the transit. A value of one corresponds to the center of the planet grazing the limb of the star at the midtime of the transit. Impact parameter affects the shape of the light curve and is influential in determining whether the light curve will have a flattened bottom surrounding the transit midtime.

Limb Darkening

The disk of a star appears dimmer near the limb than near the center. This phenomenon is known as *limb darkening*. It occurs because the length of one optical depth penetrates more deeply into the stellar envelope (and therefore to hotter, brighter material) when it "pokes" into the star at a right angle than at a grazing angle. The parameters u and v are used in modeling this effect (see appendix C). The effect this phenomenon has on a light curve is similar to, and can be confused with, that of the impact parameter.

Scale

The *scale* is the average ratio of the target star to the comparison star in the baseline part of a light curve (i.e. when a transit is not occurring). The scale is affected by the manner in which photometry is performed. The use of a new comparison star or of a different aperture size can cause the scale to change. The scale can also be affected by problems in data collection and calibration. If the images used to generate light curves are not perfectly flat-fielded, a number of otherwise minor changes can cause significant changes in scale. For example, the stars of interest may not be positioned on the same detector pixels from data set to data set (which is nearly unavoidable), causing a change in scale from data set to data set.

Slope

If such changes in scale occur (due to a combination of imperfect flat-fielding and imperfect telescope tracking or due to some other cause) within data sets (rather than just between data sets), the result is that an artificial trend is introduced into the data. The baseline component of a light curve, for example, might cease to appear flat even if no variation in the magnitude of the target and comparison stars actually occurred while those points were being recorded. One way of *detrending* such data is to introduce a new parameter, *slope*. Slope is the rate at which data points are allowed to vary linearly with some other recorded value such as time, airmass, or the x or y position of the stars on the detector.

Midtime

The transit *midtime* is the point in time at which the centers of the disks of the transiting planet and host star make their closest approach to one another. This is the parameter of greatest importance to this research.

6.2.2 How the Parameters are Used

In any given fitting session eight parameters are either held constant or varied: scale, slope, midtime, radius ratio, impact parameter, and the two limb-darkening parameters u and v. The quality of the data was not high enough to permit fitting for u and v. In all cases u and v were held constant at 0.73 and -0.22, respectively, these being roughly appropriate values for the wavelength band in which observations were made. The other six parameters were either held constant or varied based on the type of fit being performed.

6.3 Types of Fits

Two broad categories of fit are possible. In an *individual* fit, a separate model light curve is fit to each night of data.The important feature of an individual fit is that all of the data points used in the fit are from the same night. In a *joint* fit, a single model light curve is fit to all nights of data at once, generating a set of model light curve parameters which fit all of the data sets as well as possible. Data points from all nights are used in the fit.

6.4 Procedure for Individual Fitting

6.4.1 Setup

A particular data set is selected. Another round of data selection is performed to ensure that clearly-outlying points will not improperly affect the fit. The light curve is plotted and a list of frame numbers to reject is manually entered. The light curve is then replotted without those points. This process is repeated if necessary. For two reasons, the light curve is then binned. Binning averages away some of the scatter in the light curve. Binning also reduces the number of data points to which a light curve must be fit, dramatically reducing the required computing time. The light curve is plotted again and is used to manually (and roughly) estimate the scale and midtime

of the light curve. These will be used as starting values of scale and midtime when the fitting code is run. Literature values will be used as starting values for most other parameters.

6.4.2 The Fit

Values published in a chosen reference paper are used as starting values for most parameters. Rough estimates of scale and midtime have already been entered manually. A rough estimate of slope can be entered (though this proved unnecessary). A model light curve using these starting values is plotted over the data to allow visual confirmation that the model is close to the data. The fitting process itself is then performed. Selected model light curve parameters are varied iteratively and compared to the data in order to minimize χ^2 (the squared sum of the residuals). When the amount of reduction in χ^2 per iteration falls below a specified limit, or when a specified number of iterations is reached, the fitting is halted. This process is then repeated (possibly with a different set of parameters) if needed. The parameters of the fitted model light curve are then exported to disk.

6.5 Procedure for Joint Fitting

In joint fitting, different parameters are treated differently. Radius ratio, impact parameter, and duration (the real-world values of which should be the same across multiple transits of a given planet) are held to the same values across the five data sets. Scale is expected to vary from data set to data set (due to changes in airmass or choice of comparison star) and so the scales of the five data sets are treated as five independent parameters in the joint fit. The most important parameter is midtime. The period between successive midtimes can vary from data set to data set (and the goal of this research is to uncover such timing variations) and so the midtimes of the five data sets are also treated as five independent parameters in the joint fit.

6.6 Results

All fitting was performed in Mathematica using a notebook written by Elisabeth Adams [1]. Two sets of individual fits were performed, followed by a joint fit.

In all cases fitting was performed using binned data. The fitting process was sufficiently time-consuming using binned data that the amount of computing time required to fit to unbinned data would have been prohibitively large. In addition, fitting to unbinned data was not expected to significantly decrease the uncertainty of the fitted transit midtimes, which were the most important quantities to be determined. The typical bin was roughly five minutes wide and included between roughly three and sixty unbinned points, depending on the night.

6.6.1 Individual Fit Set 1: Five Free Parameters

In the first set of individual fits, five parameters were varied: scale, midtime, duration, radius ratio, and impact parameter. Slope was fixed at zero for all data sets. The resulting fitted model light curves are shown in figures B-22, B-23, B-24, B-25, and B-26. The fit parameters and their errors are shown in tables A.5, A.6, A.7, A.8, and A.9.

6.6.2 Individual Fit Set 2: Two Free Parameters

In the second set of individual fits, two parameters were varied. Each data set was fit separately for scale and midtime. All other values were held constant during fitting, with the same constant values being used for each of the five individual fits. Slope was fixed at zero for all data sets. Duration was held constant at a value derived using quantities reported by Sozzetti et al. (2008) [8]. Impact parameter was held constant at a value reported by Sozzetti et al. (2008). Radius ratio was held constant at a value derived (due to an error) using a planetary radius reported by O'Donovan et al.[5] and a stellar radius reported by Sozzetti et al. (2008) (this error likely accounts for the overall difference in results between this fitting method and the other two fitting methods). The resulting fitted model light curves are shown in figures B-27, B-28, B-29, B-30, and B-31. The fit parameters and their errors are

34

shown in tables A.10, A.11, A.12, A.13, and A.14.

Literature or literature-derived values of radius ratio, impact parameter, and duration were used in this set of fits because the actual values of these parameters (unlike midtime and scale) must be the same from one transit event to the next. In addition, due to the variation (from night to night) of the shape of the five light curves used in fitting and the noisiness of some of the light curves, literature or literature-derived values of radius ratio and impact parameter were expected to be more reliable than fitted values.

6.6.3 Joint Fit

The data sets were individually fit for their respective scales and midtimes (ten parameters) and then fit again for their midtimes only (five parameters).

Radius ratio, impact parameter, and duration were held to the same values across the five data sets. The values of these three parameters used were those determined by the individual, five-free-parameter fit to the 20080904 data set (the full output of which is shown in table A.8) as this data set contained extensive pre-ingress and post-egress baseline data and did not contain any unusual noise patterns.

The resulting fitted model light curves are shown together in figure B-32. The fit parameters and their errors are shown in table A.15.

This fit was accomplished in several steps. In the second-to-last step the five light curves were fit simultaneously for midtime and full scale. In the last step the five light curves were fit for midtime only. The midtime errors shown here are from the output of the last fitting step. The full scale errors shown here are from the output of the second-to-last fitting step (full scale errors were not printed by the output of the second fitting step because errors are only printed for the parameters being fit in a particular step). Any resulting inaccuracy in the full scale errors shown in table A.15 is expected to be very minor and should not have any impact on the midtimes or midtime errors shown in table A.15 or on the O-C plots included elsewhere in this work.

Chapter 7

Analysis

The transit midtimes determined by the three fitting methods were each compared to a published ephemeris. Projected transit midtimes, generated using the period and (the earliest of the) transit midtimes published by Sozzetti et al. (2008) [8], were subtracted from the fitted transit midtimes (from this research) and from the remainder of the transit midtimes published by Sozzetti et al. The resulting time differences represent the transit timing variation (TTV) of each transit event and are visualized using plots of "observed-minus-calculated" ("O-C") transit midtime.

Selected parameters published by O'Donovan et al. (2007) [5] and Sozzetti et al. (2008) are reproduced in tables A.16 and A.17. Midtimes published by Sozzetti et al. (2008) are reproduced in table A.18.

7.1 Plots of Observed Transit Time Variation

The midtimes from Sozzetti et al. (2008) are plotted alone in figure B-33. The midtimes output by individual fit set 1 (in which five parameters were allowed to vary) are plotted alongside the midtimes from Sozzetti et al. in figure B-36. The midtimes output by individual fit set 2 (in which only scale and midtime were allowed to vary) are plotted alongside the midtimes from Sozzetti et al. (2008) in figure B-37. The midtimes output by the joint fit (in which the scales and midtimes for all five data sets were allowed to vary individually while all other parameters were held constant

37

across all data sets) are plotted alongside the midtimes from Sozzetti et al. (2008) in figure B-38. The midtimes output by all three fitting methods are plotted together in figure B-34. The midtimes output by all three fitting methods are plotted alongside the midtimes from Sozzetti et al. (2008) in figure B-35.

7.2   Discussion

7.2.1   Comparison of Fitting Methods

The midtimes output by the individual, five-free-parameter fitting method and the joint fitting method are very similar across all five data sets. The midtimes output by the individual, two-free-parameter fitting method are consistently different from those of the other two methods across all five data sets. This difference is due mostly to an error made when the non-free parameters in the two-free-parameter fitting method were derived from literature values. The error is described in more detail in section 6.6.2. For each of the five nights, the error bars of the two-free-parameter fitting method overlap with the error bars of the other two methods. The results of the two-free-parameter fitting method are nevertheless less trustworthy that the results of the other two methods and so are rejected.

The error bars of all five midtimes output by the joint fitting method overlap near an O-C of 125 s (which is roughly the O-C of the fourth night). This occurs largely because the midtimes from three of the nights (the first, fourth, and fifth) are significantly uncertain. The error bars of the midtimes output by the individual, five-free-parameter fitting method are generally smaller, with only the fifth night having a large uncertainty, and with that midtime being centered near an O-C of zero. As a result, the remainder of this analysis will focus on the output of the individual, five-free-parameter fitting method, which will now be referred to as the *fit midtimes*. As the nominal midtimes output by these two fitting methods are very similar, it is believed that this simplification can be made without loss of insight.

7.2.2 Comparison to Literature Midtimes

Four of the five fit midtimes have error bars which overlap (or nearly overlap) the error bars of the midtimes from Sozzetti et al. The fit midtime from the first night, however, has an O-C of roughly 325 s – much larger than those of the other fit midtimes and the literature midtimes. As is pointed out in section 2 of Steffen & Agol (2005) [9], it is points like this which are of greatest interest. In the following section, the mass, eccentricity, and period-ratio parameter space of two published transit timing models is explored in order to use this point to constrain the properties of a potential perturbing body in the TrES-3 system.

7.3 Interpretation of the Midtime from Night 1

In an effort to understand the possible significance of the aberrant midtime, TTV models from Holman & Murray (2005) [4] and Agol et al. (2005) [2] were applied to the TrES-3 system and explored. Using each model, a variety of perturbing-body masses, eccentricities, and period ratios (ratios of the orbital period of the perturbing body to that of TrES-3) were selected. The resulting TTVs were calculated and discussed. In all cases the perturbing body was assumed to have an orbital period longer than the 1.3 day period of TrES-3. Orbits inferior to that of the massive, short-period TrES-3 are unlikely to be stable in the long term and so were not explored.

7.3.1 Model #1 Test Cases

Equation 1 of Holman & Murray (2005) was used to explore a set of test cases.

Low Eccentricity, 1 M_{Earth}

Figure B-39 shows the TTV resulting from a perturbing mass of 1 M_{Earth} at a range of eccentricities from 0.1 to 0.5 and at a range of period ratios. None of the combinations of eccentricity and period ratio plotted are more than marginally detectable given the timing precision of the data in this work. Note that the curves corresponding

to eccentricities of 0.4 and 0.5 have positive slope on the left-hand side of the plot. This is likely due to a combination of small period ratio and moderate eccentricity causing the orbit of the perturber to cross that of TrES-3. Such a configuration is only possible if the two bodies are in a mean-motion resonance; this configuration is dealt with in section 7.3.3 and so these portions of the curves are left out of the analysis in this section.

Low Eccentricity, 10 M_{Earth}

Figure B-40 shows the TTV resulting from a perturbing mass of 10 M_{Earth} at a range of eccentricities from 0.1 to 0.5 and at a range of period ratios.

Note that in the top plot in figure B-40 the curves corresponding to eccentricities of 0.4 and 0.5 have positive slope on the left-hand side of the plot. As before, this is likely due to a combination of small period ratio and moderate eccentricity causing the orbit of the perturber to cross that of TrES-3. These sections of the curves are unphysical given that the model used in this test case applies only to non-resonant perturbers. For the non-resonant case, then, there is a maximum possible eccentricity for a given period ratio (and perturber mass).

The bottom plot in figure B-40 shows the same curves plotted over a different range of period ratios such that the unphysical behavior in the top plot is avoided. This plot suggests that a 10 M_{Earth} body with any eccentricity is detectable given the timing precision of the data in this work. As eccentricity increases, however, period ratio must increase as well to prevent a disastrous non-resonant crossing of the orbits of the perturber and TrES-3 (and to keep the resulting TTV from growing beyond values consistent with what was observed).

Low Eccentricity, 1 M_J and 10 M_J

Figure B-41 shows the TTV resulting from perturbing masses of 1 and 10 M_J at a range of eccentricities from 0.1 to 0.5 and at a range of period ratios.

The top plot in figure B-41 suggests that a non-resonant 1 M_J body with a period ratio below roughly 3.5 and with any eccentricity results in a TTV far larger than

what was observed. As eccentricity increases, the minimum consistent period ratio increases as well. The bottom plot in figure B-41 suggests that a non-resonant 10 M_J body with a period ratio below roughly 8 and with any eccentricity results in a TTV far larger than what was observed. As before, as eccentricity increases, the minimum consistent period ratio increases as well.

7.3.2 Model #2 Test Cases (No Resonance)

A model described in part 4 of Agol et al. (2005) was used to explore a set of test cases in which the perturbing planet was in a much larger orbit than TrES-3. The model is only applicable to large period ratios and makes the assumption that resonances can be safely ignored. In these test cases period ratios smaller than 10 were therefore not considered.

Low Eccentricity

Figure B-42 shows the TTV resulting from perturbing masses of 1, 10, and 100 M_J at a range of eccentricities from 0.1 to 0.5 and at a range of period ratios. Comparison of the three plots reveals that the TTV scales linearly with the mass of the perturber.

The top plot in figure B-42 suggests that a 1 M_J perturber at low-to-moderate eccentricity is not detectable given the timing precision of the data in this work. The middle plot in figure B-42 suggests that a 10 M_J perturber at low-to-moderate eccentricity is only marginally detectable, at best, given the timing precision of the data in this work. The bottom plot in figure B-42 suggests that a 100 M_J perturber could be detectable given the timing precision of the data in this work. A body of that mass at eccentricity 0.5 and a period ratio not far above 10 would result in a TTV consistent with the observed TTV. It is likely, though, that a body that massive (such as a large brown dwarf) would already have been detected via radial velocity measurements.

41

High Eccentricity

Figure B-43 shows the TTV resulting from perturbing masses of 100 M_{Earth}, 1 M_J, and 10 M_J at a range of eccentricities from 0.5 to 0.9 and at a range of period ratios.

The top plot in figure B-43 suggests that a 1 M_{Earth} body, at any eccentricity, is not detectable given the timing precision of the data in this work. The middle plot in figure B-43 suggests that a 1 M_J (roughly 317 M_{Earth}) body at very high eccentricity and a period ratio not far above 10 is only marginally detectable, at best, given the timing precision of the data in this work. The bottom plot in figure B-43 suggests that a 10 M_J body at high eccentricity is detectable given the timing precision of the data in this work. A body of that mass at an eccentricity near 0.9 and a period ratio not far above 10 would result in a TTV consistent with what was observed.

Figure B-44 shows the TTV resulting from a perturbing mass of 100 M_J at a range of eccentricities from 0.5 to 0.9 and at a range of period ratios. Such a body at high eccentricity is detectable given the timing precision of the data in this work. To be consistent with the observed TTV a perturber with eccentricity 0.5 would need a P/P not far above 10, a perturber with eccentricity 0.8 would need a period ratio of roughly 40, a perturber with eccentricity 0.85 would need a period ratio of roughly 70, and a perturber with eccentricity 0.9 would need a period ratio of roughly 140.

7.3.3   Model #3 Test Cases (Resonance)

A model described in part 6 of Agol et al. (2005) was used to explore a set of test cases in which a perturber is in a j:j+1 mean-motion resonance with TrES-3. Resonances become less significant as j grows and so values of j above 10 were not considered.

Figure B-45 shows the TTV, as a function of j, resulting from perturbing masses of 1 M_{Earth}, 10 M_{Earth}, 50 M_{Earth}, 100 M_{Earth}, and 317 M_{Earth} (roughly 1 M_J).

The top plot in figure B-45 illustrates the dependence of TTV on j. The middle plot in figure B-45 suggests that the observed TTV could be accounted for by a 10 M_{Earth} perturber in a 2:1 resonance with TrES-3. The bottom plot in figure B-45 suggests that the observed TTV could be accounted for by a 50 M_{Earth} perturber in a

roughly 6:7 resonance with TrES-3 and could nearly be accounted for by a 100 M_{Earth} perturber in a roughly 10:11 resonance.

7.4 Conclusion

7.4.1 In Brief

Exploration of the mass/eccentricity/period-ratio parameter space suggests that the roughly 30-second peak timing precision achieved during this work (on 20080827) is sufficient to detect large perturbing objects in transiting systems.

The single large TTV ($\sim$325 s) observed on 20080711 appears insufficient to constrain the properties of a prospective third body in the TrES-3 system. The remaining transit midtimes, while corresponding to much smaller TTVs, are not numerous enough (and densely-spaced enough) to constrain the properties of a third body. The observed TTVs are, however, consistent with the presence of a low-mass body in mean-motion resonance with TrES-3, leaving TrES-3 as a worthy candidate for further transit observations.

7.4.2 What is Needed

More data points are needed. First, TTV signals need not be well-behaved sinusoids, making it difficult to find periodicity in a handful of data points. Second, a wide variety of combinations of perturber mass and orbital parameters can explain the observation of a single large TTV, making it difficult to constrain perturber mass or orbital elements even in the presence of a single significant TTV detection.

Other researchers appear to agree that transit timing studies are data-hungry. At the end of their numerical study of the general transit timing problem, Veras & Ford (2009) [10] state that "for certain orbital configurations, as few as 10 transit detections may be able to constrain TTV profiles well enough to place useful constraints on the orbital parameters of a possible external perturber." If this is true, then in the best case, the quantity of data used in this work is only barely

sufficient. And in section 3.1 of their transit timing study of TrES-1, which made use of 12 transit midtimes including one midtime possibly representing a large TTV, Steffen & Agol (2005) state that "we conclude that there is not sufficient information in the data to determine the characteristics of a secondary planet in the TrES-1 system uniquely and satisfactorily."

7.4.3 Future Work

There are ways, in addition to simply observing more transits, for transit timing researchers to optimize their observing programs.

First, study known transiting planets with the longest available orbital periods (e.g. HD80606b, period $\sim$111 days, and HD17156b, period $\sim$21 days). This allows a given perturber-induced stellar displacement to correspond to a larger TTV [4]. As timing precision is independent of TTV size, an amplified TTV signal provides a detection with a higher signal-to-noise ratio.

Second, observe as many consecutive transits as possible. This can be accomplished by observing from sites which are distributed in longitude. This can also be accomplished through careful planet selection. Transiting planets with orbital periods which are nearly integer multiples of the solar day are able to provide observable transits many nights in a row. Observation of consecutive transits allows the detection of short-libration-period TTV signals that would be overlooked by intermittent observations.

Appendix A

Tables

Table A.1: Observatories

Site	Aperture	Pixel Scale	Field Size	Filters	Comments
WAO	0.6 m	0".36/pixel	3' 1"	700nm LP, Rs	Unstable guiding.
IRTF	3.0 m	0".12/pixel	1' 1"	700nm LP	Variable flat-fielding.

Table A.2: Observation Nights

Night	Site	Filter*	Frames	Integration Time (s)	Flats Recorded?
20080711	WAO	700nm LP	300	60	Dawn sky (after event)
20080823	IRTF	700nm LP	740	10	Dome (after event)
20080827	IRTF	700nm LP	1160	10	Dome (before/after event)
20080904	WAO	Rs	120	120	Sky (20080906)
20080921	WAO	Rs	120	120	Dusk sky (before event)

*See sections 2.3.1, 2.4.1.

Table A.3: Flat-Fielding

Night	Site	Comments
20080711	WAO	Flat-fielded using sky flats recorded on same night.
20080823	IRTF	Initially flat-fielded using dome flats recorded on same night. Results unsatisfactory. Ultimately flat-fielded using sky flats recorded on 20080907. Results still incompletely-flattened.
20080827	IRTF	Initially flat-fielded using dome flats recorded on same night. Results unsatisfactory. Ultimately flat-fielded using sky flats recorded on 20080907. Results still incompletely-flattened.
20080904	WAO	Flat-fielded using sky flats recorded on the night of 20080906.
20080921	WAO	Flat-fielded using sky flats recorded on the same night.

Table A.4: The best aperture-photometry box sizes for the individual nights are listed. Also listed are the figure numbers of the best-box-size light curves, the light curves at all box sizes (plotted together for comparison), and other quantities.

Night	Best Box Size (pixels)	Light Curve at Best Box Size	Light Curves at All Box Sizes	Other Interesting Quantities
20080711	25	Figure B-6	Figure B-11	Figure B-16
20080823	35	Figure B-7	Figure B-12	Figure B-17
20080827	35	Figure B-8	Figure B-13	Figure B-18
20080904	20	Figure B-9	Figure B-14	Figure B-19
20080921	25	Figure B-10	Figure B-15	Figure B-20

Table A.5: Results of individual, five-free-parameter fit, 20080711. Parameters in **boldface** were held constant during the fitting process.

Parameter	Value	Fit Error
fullScale	2.0072	0.0012
fullScaleSlope	**0**	
transitMidtime (MJD)	54658.25341	0.00080
totalDuration (days)	0.0577	0.0041
radiusRatio	0.167	0.028
impactParam	0.847	0.088

46

Table A.6: Results of individual, five-free-parameter fit, 20080823. Parameters in **boldface** were held constant during the fitting process.

Parameter	Value	Fit Error
fullScale	4.4527	0.0036
fullScaleSlope	**0**	
transitMidtime (MJD)	54701.35385	0.00046
totalDuration (days)	0.0498	0.0024
radiusRatio	0.1502	0.0053
impactParam	0.762	0.048

Table A.7: Results of individual, five-free-parameter fit, 20080827. Parameters in **boldface** were held constant during the fitting process.

Parameter	Value	Fit Error
fullScale	4.9396	0.0022
fullScaleSlope	**0**	
transitMidtime (MJD)	54705.27397	0.00030
totalDuration (days)	0.0513	0.0019
radiusRatio	0.157	0.023
impactParam	0.886	0.056

Table A.8: Results of individual, five-free-parameter fit, 20080904. Parameters in **boldface** were held constant during the fitting process.

Parameter	Value	Fit Error
fullScale	1.9121	0.0013
fullScaleSlope	**0**	
transitMidtime (MJD)	54713.11089	0.00082
totalDuration (days)	0.0475	0.0037
radiusRatio	0.1712	0.0088
impactParam	0.772	0.076

Table A.9: Results of individual, five-free-parameter fit, 20080921. Parameters in **boldface** were held constant during the fitting process.

Parameter	Value	Fit Error
fullScale	1.9013	0.0026
fullScaleSlope	**0**	
transitMidtime (MJD)	54730.0896	0.0030
totalDuration (days)	0.049	0.018
radiusRatio	0.109	0.022
impactParam	0.75	0.48

Table A.10: Results of individual, two-free-parameter fit, 20080711. Parameters in **boldface** were held constant during the fitting process.

Parameter	Value	Fit Error
fullScale	2.0114	0.0019
fullScaleSlope	**0**	
transitMidtime (MJD)	54658.2543	0.0019
totalDuration (days)	**0.081**	
radiusRatio	**0.161**	
impactParam	**0.84**	

Table A.11: Results of individual, two-free-parameter fit, 20080823. Parameters in **boldface** were held constant during the fitting process.

Parameter	Value	Fit Error
fullScale	4.4776	0.0046
fullScaleSlope	**0**	
transitMidtime (MJD)	54701.3528	0.0015
totalDuration (days)	**0.081**	
radiusRatio	**0.161**	
impactParam	**0.84**	

Table A.12: Results of individual, two-free-parameter fit, 20080827. Parameters in **boldface** were held constant during the fitting process.

Parameter	Value	Fit Error
fullScale	4.9800	0.0040
fullScaleSlope	**0**	
transitMidtime (MJD)	54705.2750	0.0012
totalDuration (days)	**0.081**	
radiusRatio	**0.161**	
impactParam	**0.84**	

Table A.13: Results of individual, two-free-parameter fit, 20080904. Parameters in **boldface** were held constant during the fitting process.

Parameter	Value	Fit Error
fullScale	1.9161	0.0017
fullScaleSlope	**0**	
transitMidtime (MJD)	54713.1115	0.0018
totalDuration (days)	**0.081**	
radiusRatio	**0.161**	
impactParam	**0.84**	

Table A.14: Results of individual, two-free-parameter fit, 20080921. Parameters in **boldface** were held constant during the fitting process.

Parameter	Value	Fit Error
fullScale	1.9089	0.0022
fullScaleSlope	**0**	
transitMidtime (MJD)	54730.0855	0.0021
totalDuration (days)	**0.081**	
radiusRatio	**0.161**	
impactParam	**0.84**	

Table A.15: Results of joint fit. Parameters in **boldface** were held constant during the fitting process. The values of duration, radius ratio, and impact parameter used were those output by the individual, five-free-parameter fit to the 20080904 data set (see section 6.6.3 for details).

Date	Parameter	Units	Value	Fit Error
All	totalDuration	days	**0.0475**	
All	radiusRatio		**0.1712**	
All	impactParam		**0.772**	
20080711	fullScaleSlope1		**0**	
20080711	fullScale1		2.0073	0.0034
20080711	midtime1	MJD	54658.2531	0.0019
20080823	fullScaleSlope2		**0**	
20080823	fullScale2		4.4614	0.0023
20080823	midtime2	MJD	54701.35400	0.00041
20080827	fullScaleSlope3		**0**	
20080827	fullScale3		4.9606	0.0026
20080827	midtime3	MJD	54705.27396	0.00043
20080904	fullScaleSlope4		**0**	
20080904	fullScale4		1.9121	0.0043
20080904	midtime4	MJD	54713.1109	0.0029
20080921	fullScaleSlope5		**0**	
20080921	fullScale5		1.9052	0.0039
20080921	midtime5	MJD	54730.0898	0.0023

Table A.16: Selected literature parameters for TrES-3. Reproduced from table 3 in O'Donovan et al. (2007) [5].

Parameter	Value
P (days)	1.30619 ± 0.00001
T_c (HJD)	2454185.9101 ± 0.0003
R_p/R_*	0.1660 ± 0.0024
$b \equiv a \cos i/R_*$	0.8277 ± 0.0097

Table A.17: Selected literature parameters for TrES-3. Reproduced from table 9 in Sozzetti et al. (2008) [8].

Parameter	Value
P (days)	1.30618581 (fixed)
T_c (HJD)	2,454,185.9104 (fixed)
R_p/R_*	0.1655 ± 0.0020
$b \equiv a \cos i/R_*$	0.840 ± 0.010

Table A.18: Literature transit midtimes for TrES-3. Reproduced from table 6 in Sozzetti et al. (2008) [8].

HJD	Uncertainty (days)	Epoch E
2454185.910430	0.000198	0
2454198.973147	0.000223	10
2454214.646298	0.000280	22
2454215.952080	0.000214	23
2454535.968246	0.000166	268
2454552.948971	0.000147	281
2454569.929089	0.000153	294
2454594.745943	0.000253	313

Appendix B

Figures

POSSII.F.DSS2.334

1'
Powered by Aladin

8.7' x 8.23'

N

E
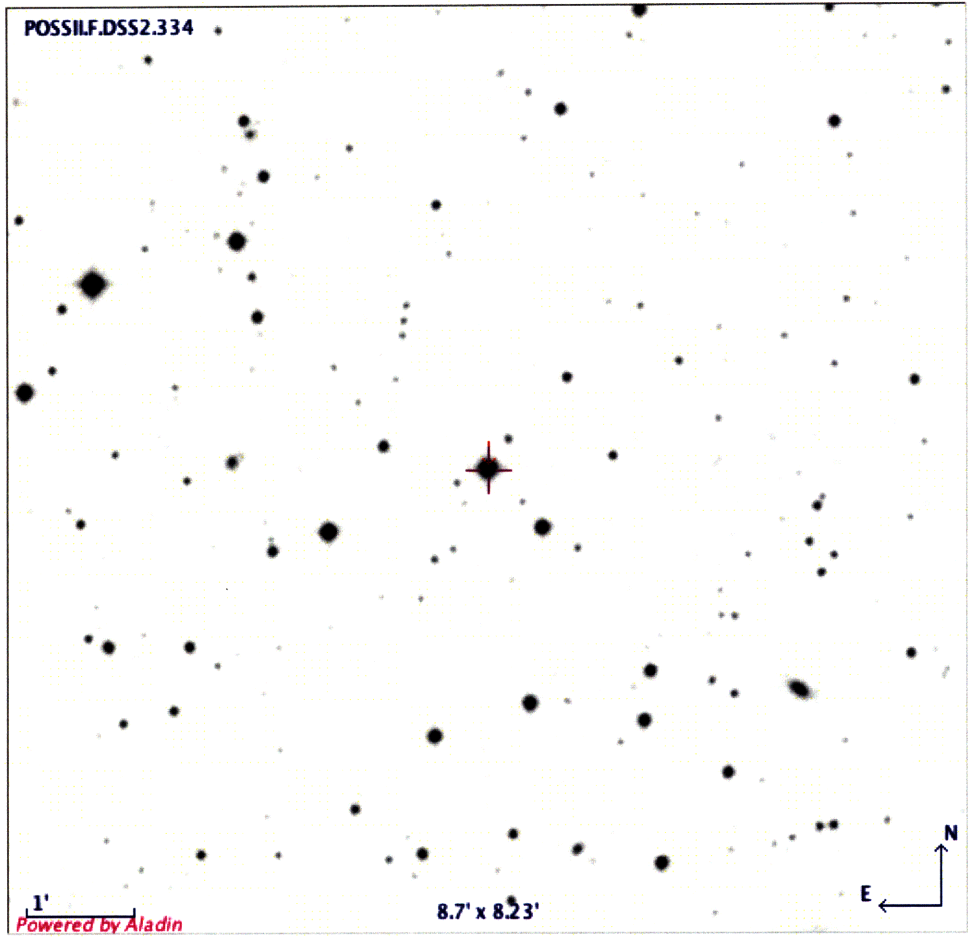
Figure B-1: Aladin [3] finder image of TrES-3 and its surroundings. TrES-3 is indicated with a crosshair and arrow.
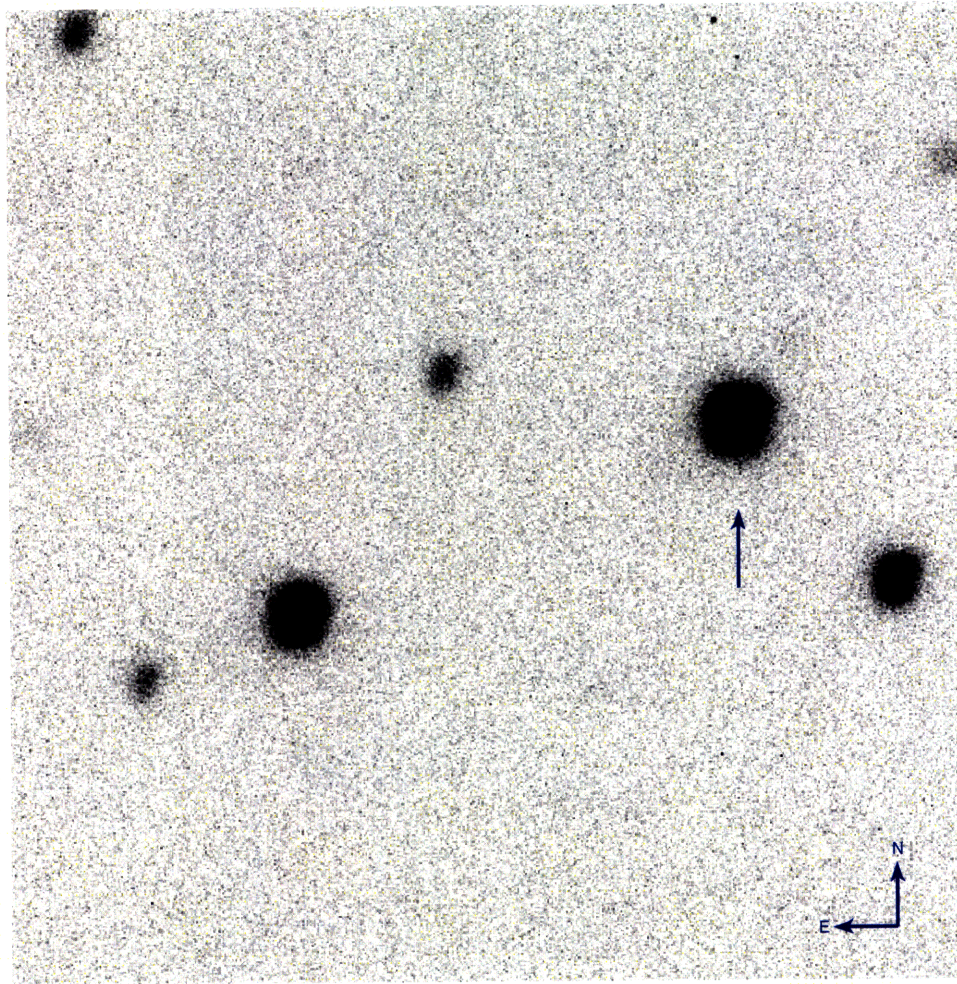
Figure B-2: Calibrated POETS image of TrES-3 field recorded at WAO. TrES-3 is indicated with an arrow. The bright object below and to the left of TrES-3 is the comparison star used to perform differential photometry on the WAO data sets. Note the steady background flux due to proper flat-fielding.
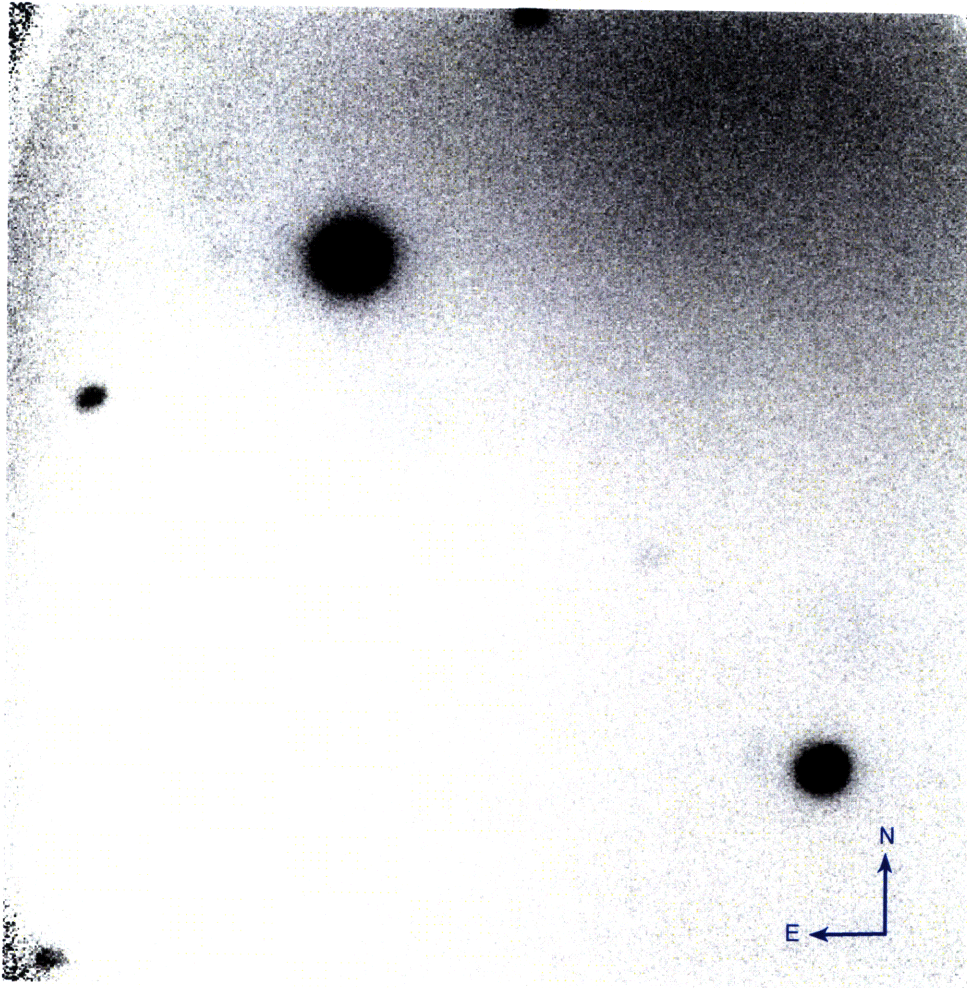
Figure B-3: Calibrated POETS image of TrES-3 field recorded at IRTF. The bright object at top left is TrES-3. The object at bottom right is the comparison star used to perform differential photometry on the IRTF data sets. Note the variation in background flux due to incomplete flat-fielding.
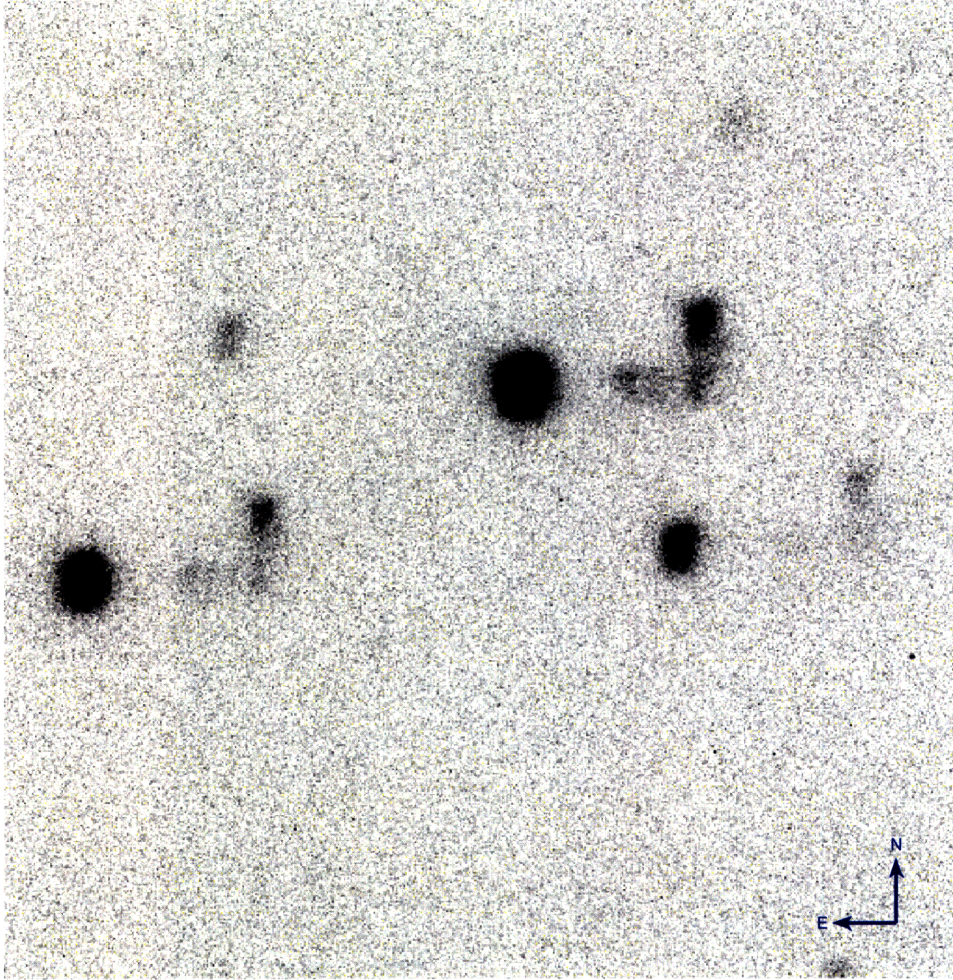
Figure B-4: Calibrated POETS image of TrES-3 field recorded at WAO. Note the effects of a manual repointing which occurred during the exposure.
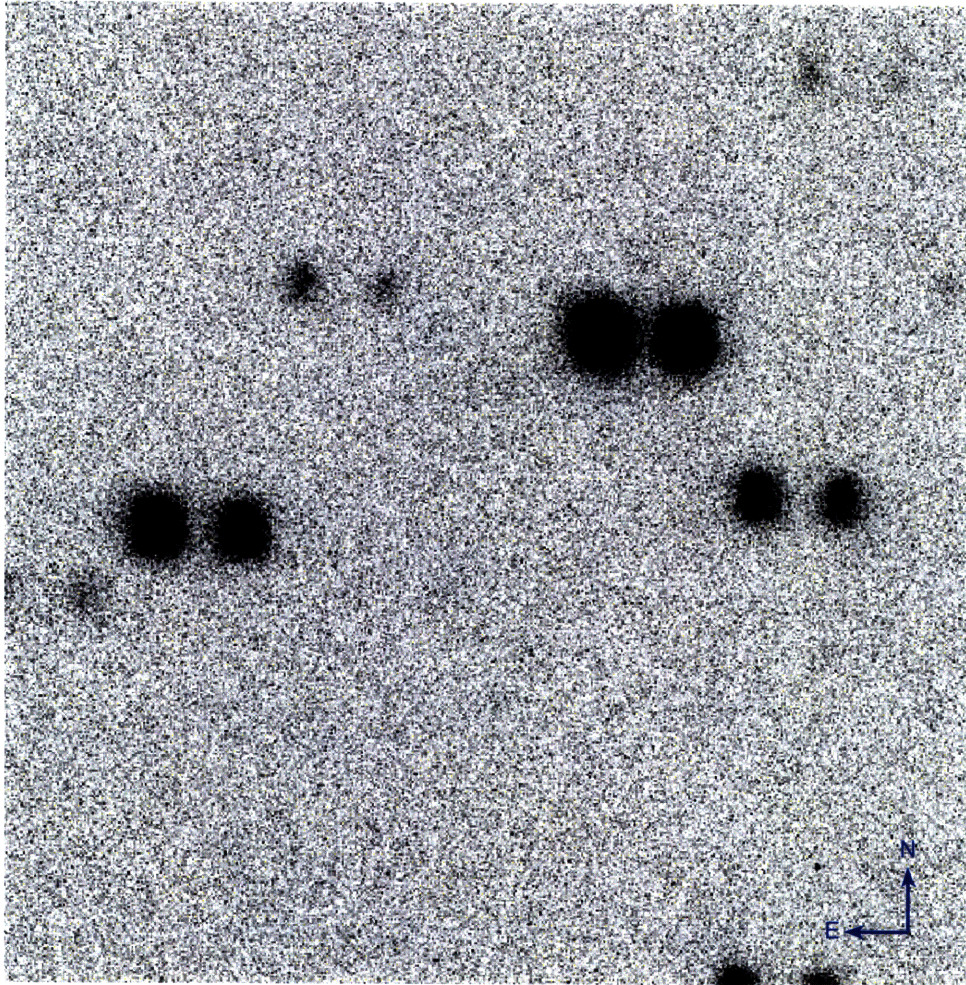
Figure B-5: Calibrated POETS image of TrES-3 field recorded at WAO. Note the effects of an unplanned pointing jump which occurred during the exposure.

TrES-3-WAO-POETS-20080711
flat-bias
25px box sd=0.0134
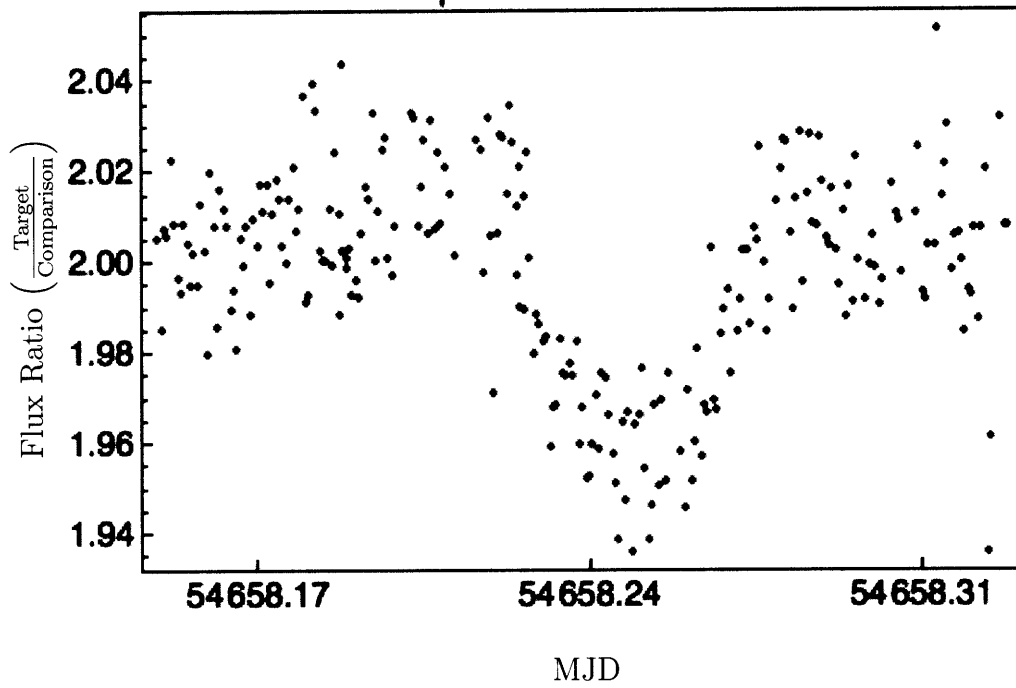
Figure B-6: Transit light curve recorded 20080711. Photometry performed with best aperture size of 25 pixels.

Figure B-7: Transit light curve recorded 20080823. Photometry performed with best aperture size of 35 pixels.

TrES-3-IRTF-POETS-20080827
flat-bias
35px box sd=0.0257
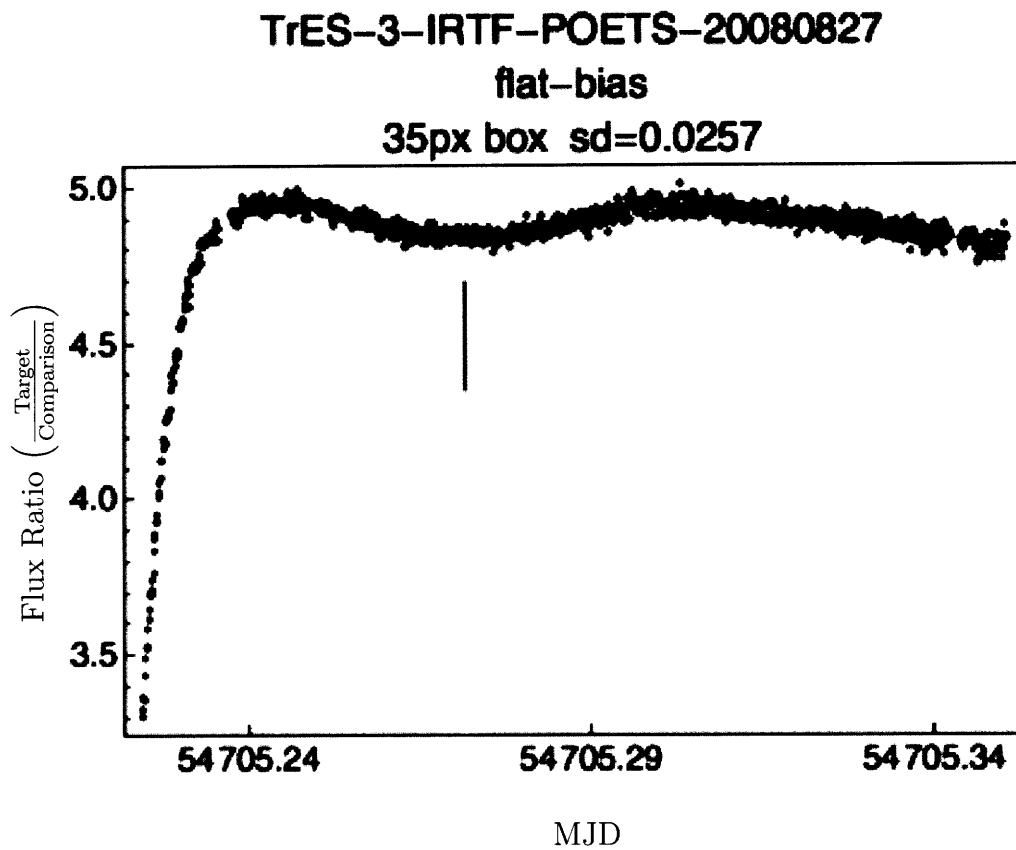
Figure B-8: Transit light curve recorded 20080827. Photometry performed with best aperture size of 35 pixels. The approximate transit midtime is indicated by a short vertical line.

TrES-3-WAO-POETS-20080904
flat-bias
20px box sd=0.00505
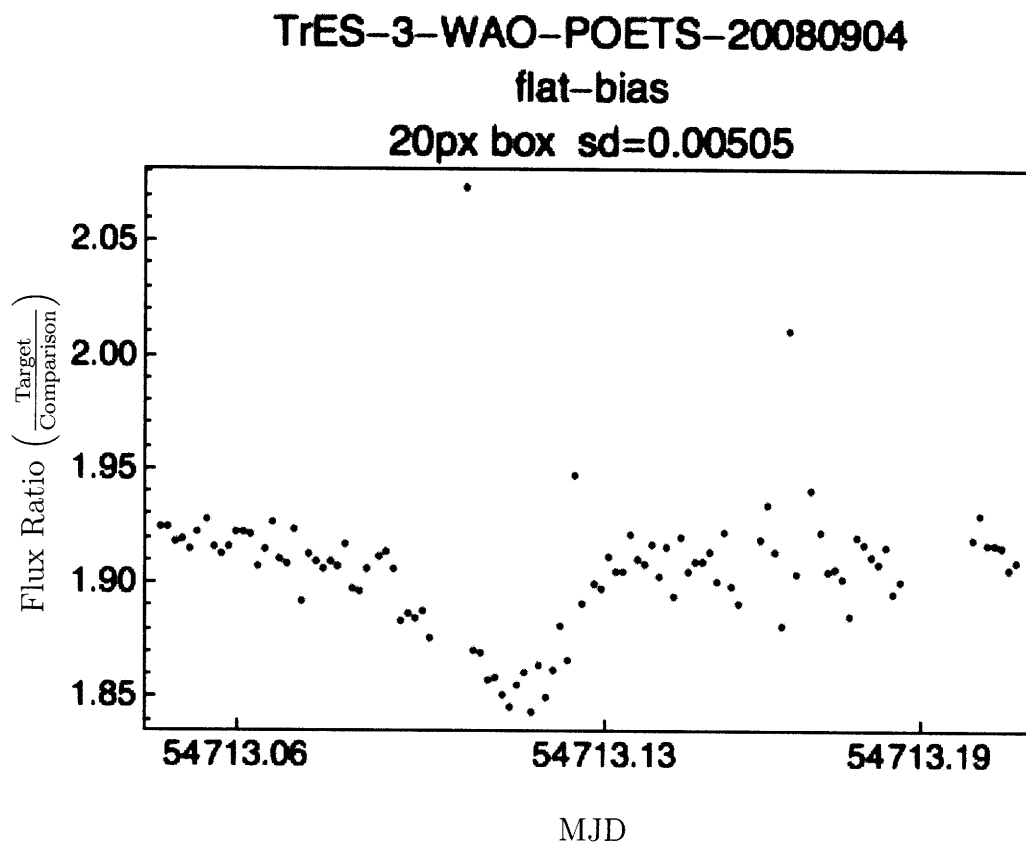
Figure B-9: Transit light curve recorded 20080904. Photometry performed with best aperture size of 20 pixels.

TrES-3-WAO-POETS-20080921
flat-bias
25px box sd=0.00596
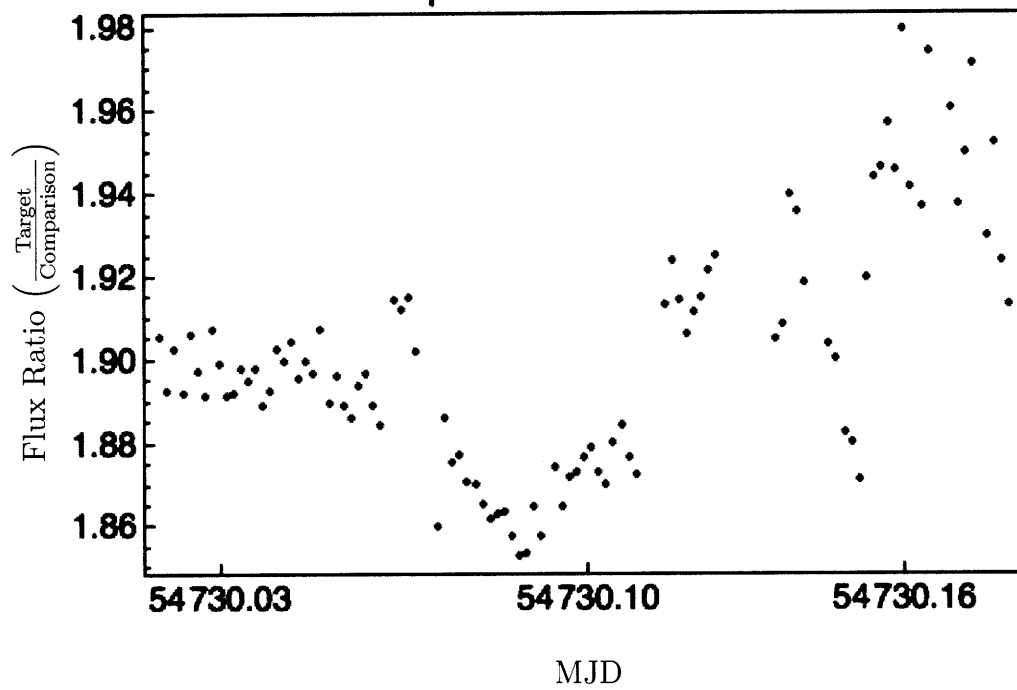
Figure B-10: Transit light curve recorded 20080921. Photometry performed with best aperture size of 25 pixels.
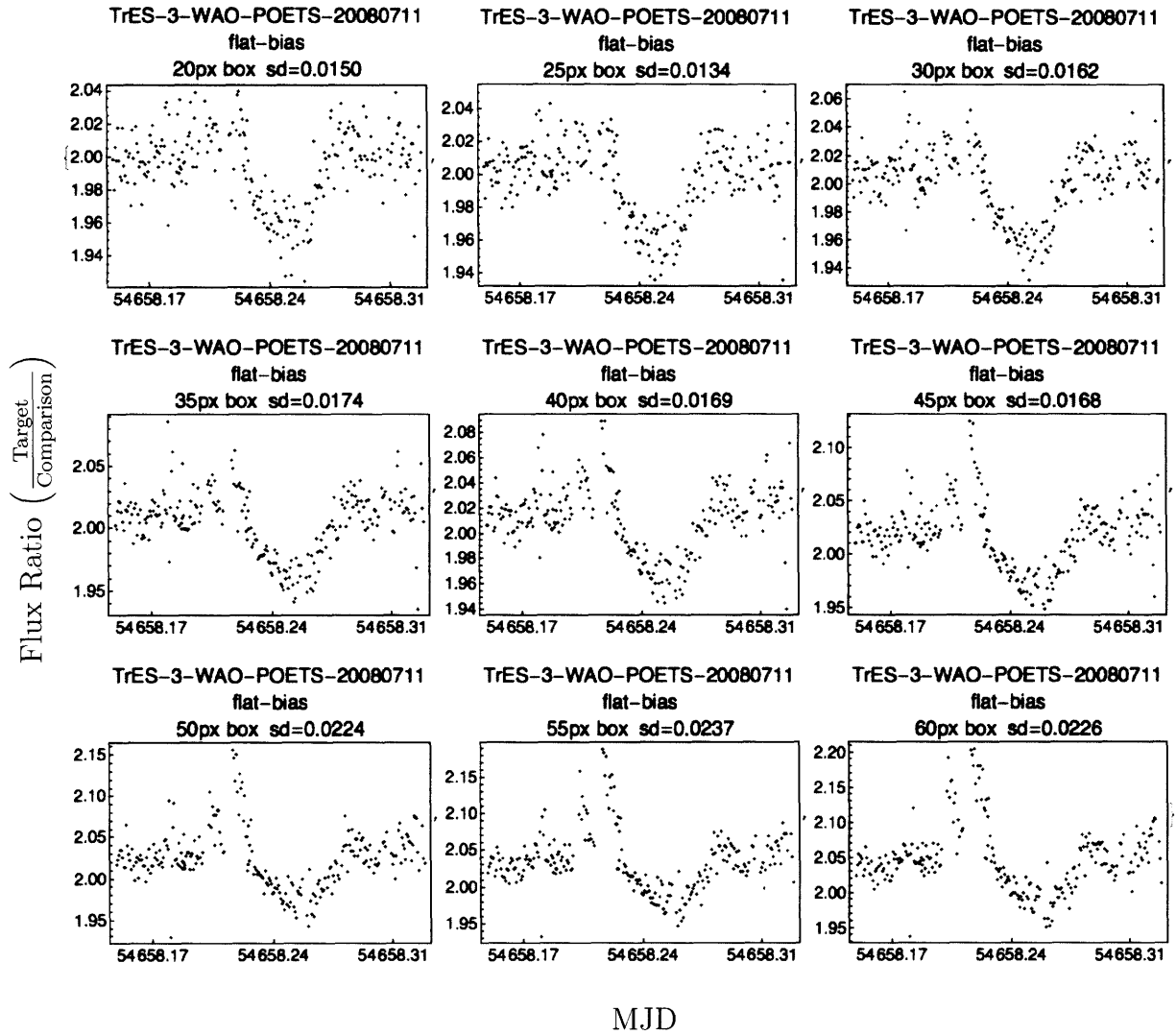
Figure B-11: Transit light curve recorded 20080711. Photometry performed with various aperture sizes.
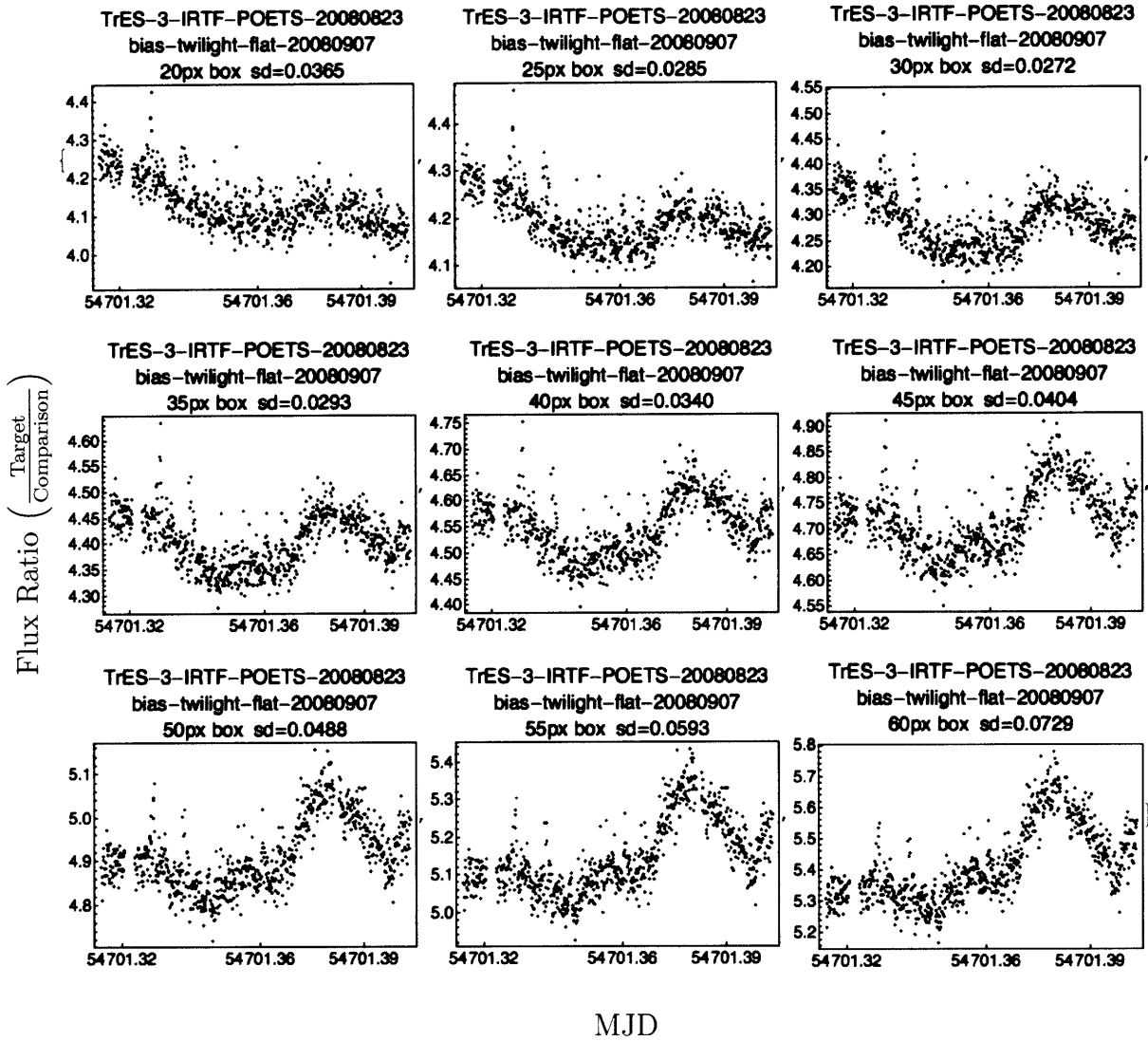
Figure B-12: Transit light curve recorded 20080823. Photometry performed with various aperture sizes.
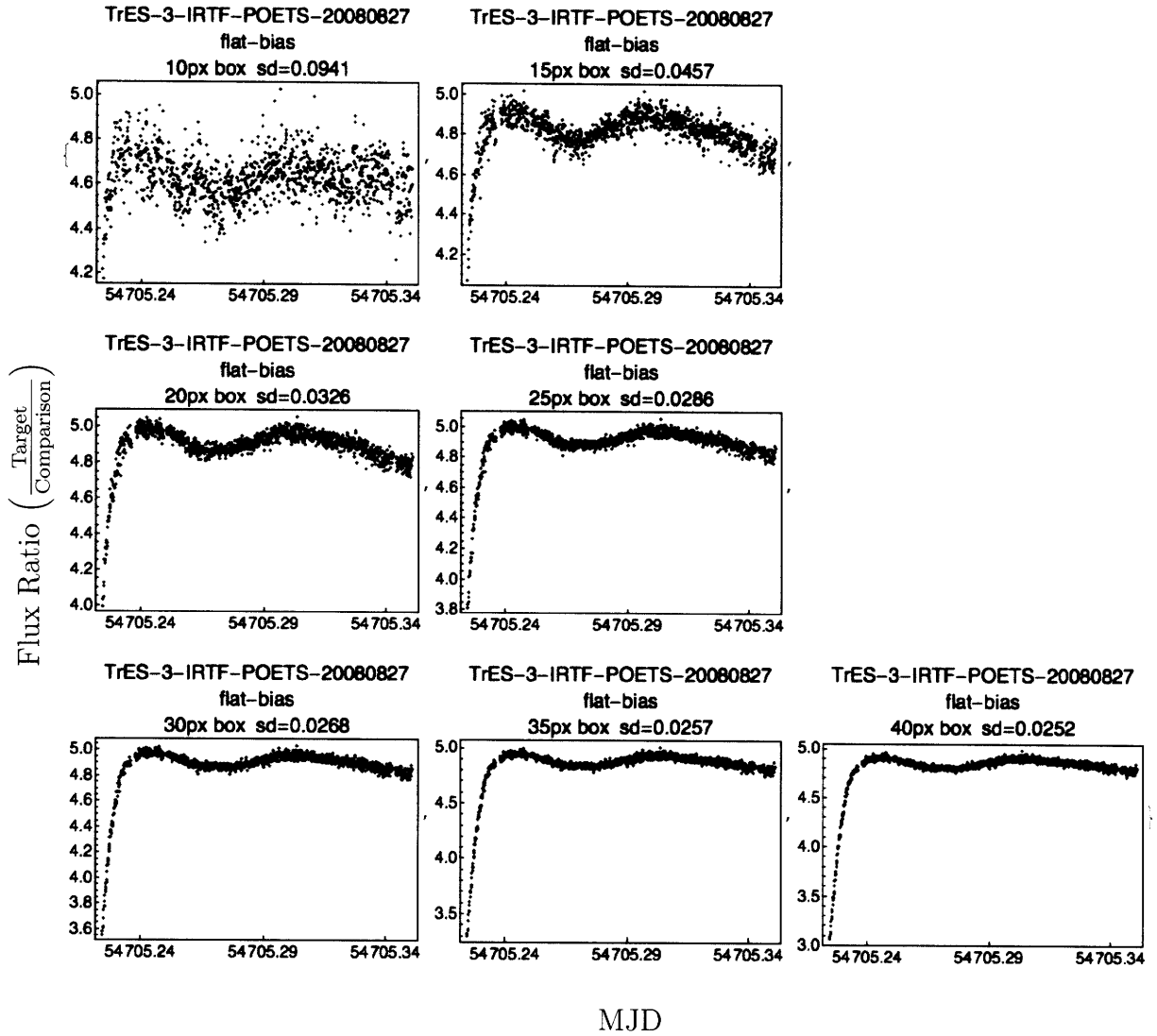
Figure B-13: Transit light curve recorded 20080827. Photometry performed with various aperture sizes.
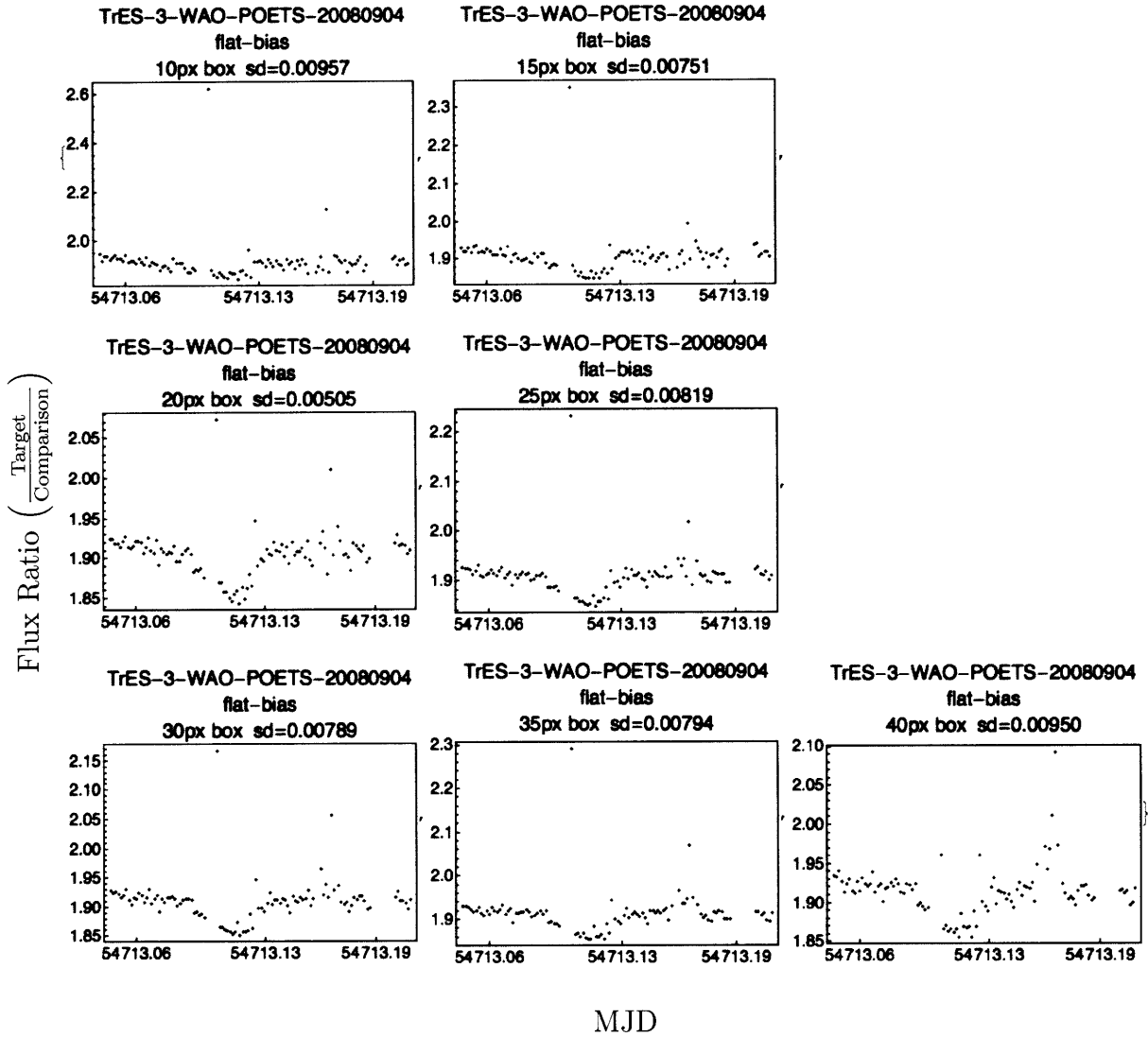
Figure B-14: Transit light curve recorded 20080904. Photometry performed with various aperture sizes.
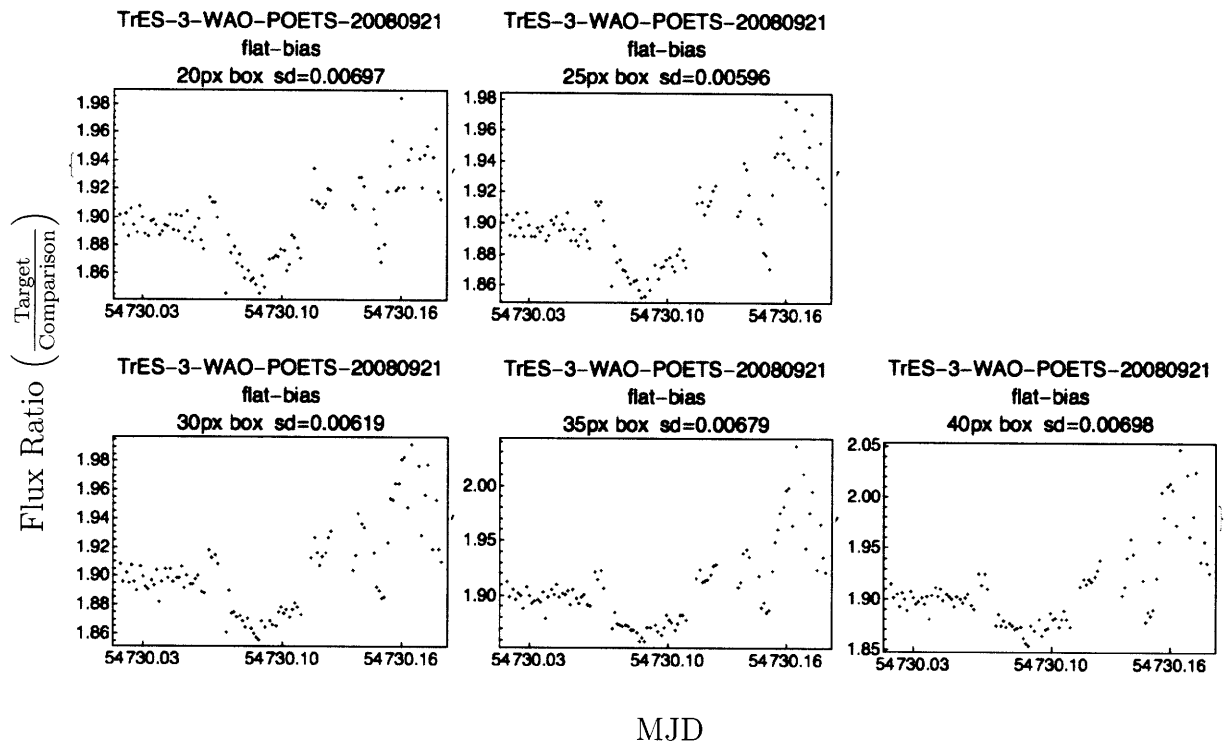
Figure B-15: Transit light curve recorded 20080921. Photometry performed with various aperture sizes.
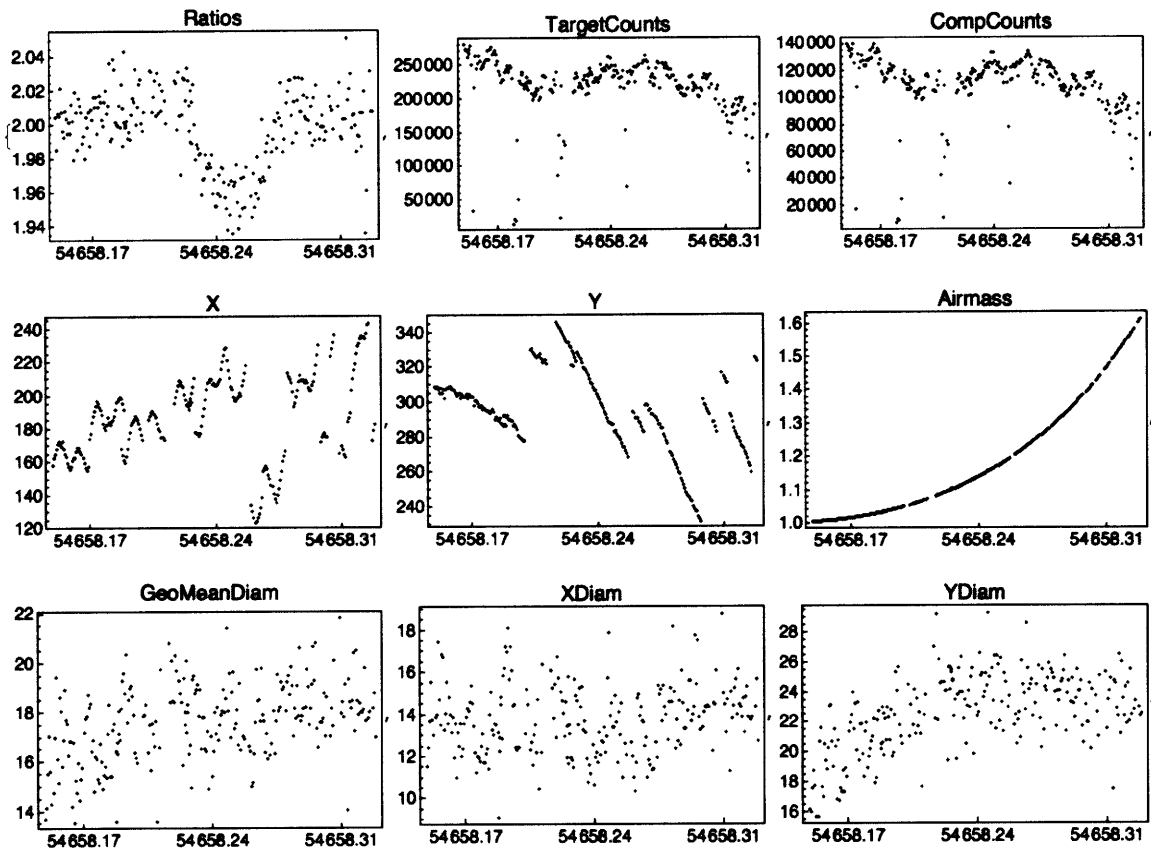
Figure B-16: Interesting quantities from 20080711 (WAO). The brief and simultaneous dips in the number of target star and comparison star counts are likely the result of clouds drifting through the field of view. The roughly fifteen-minute oscillation in the x position of the target star is caused by periodic error in the telescope mount. The jumps in the y position of the target star are caused by a combination of guiding errors and manual repointings.
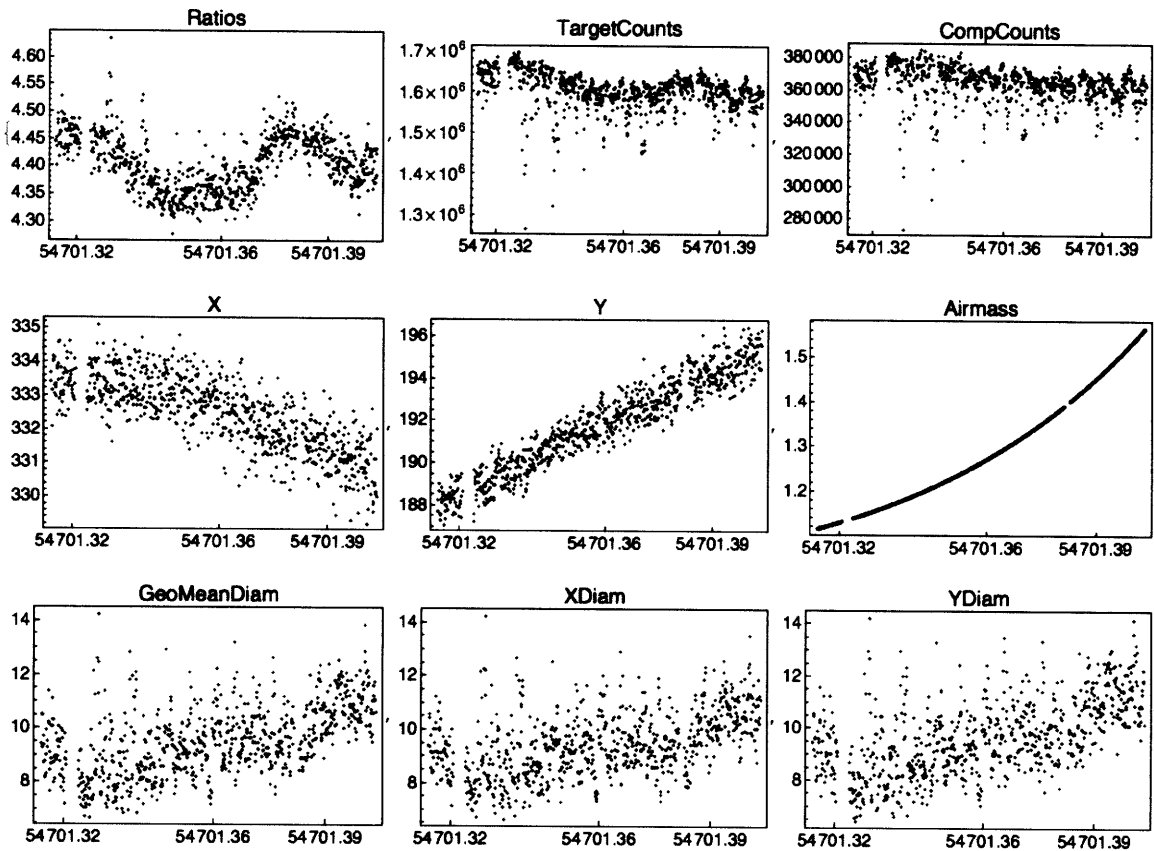
Figure B-17: Interesting quantities from 20080823 (IRTF). Note the smoothness of the guiding in the x and y directions at IRTF relative to that at WAO.
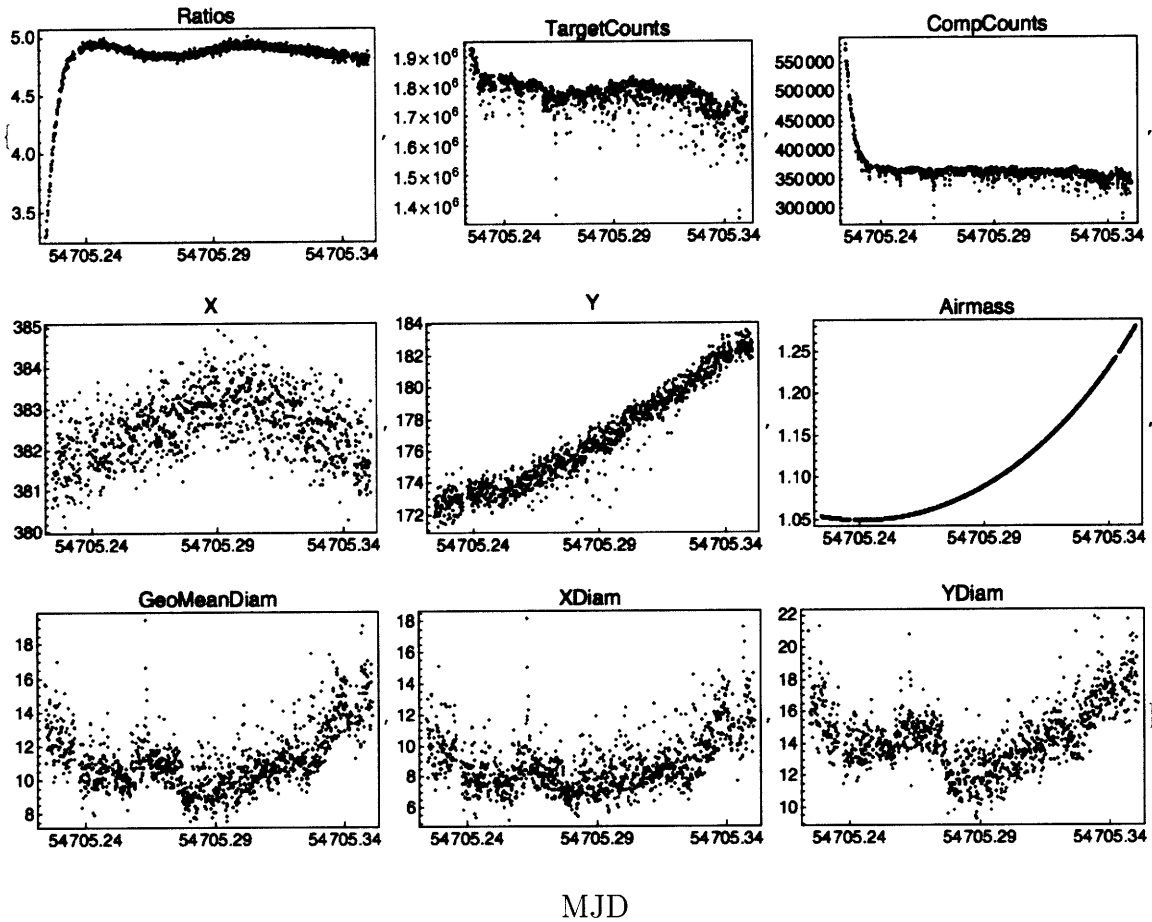
Figure B-18: Interesting quantities from 20080827 (IRTF). Note the smoothness of the guiding in the x and y directions at IRTF relative to that at WAO. Note also that the transit light curve is visible even in the plot of raw target star counts.
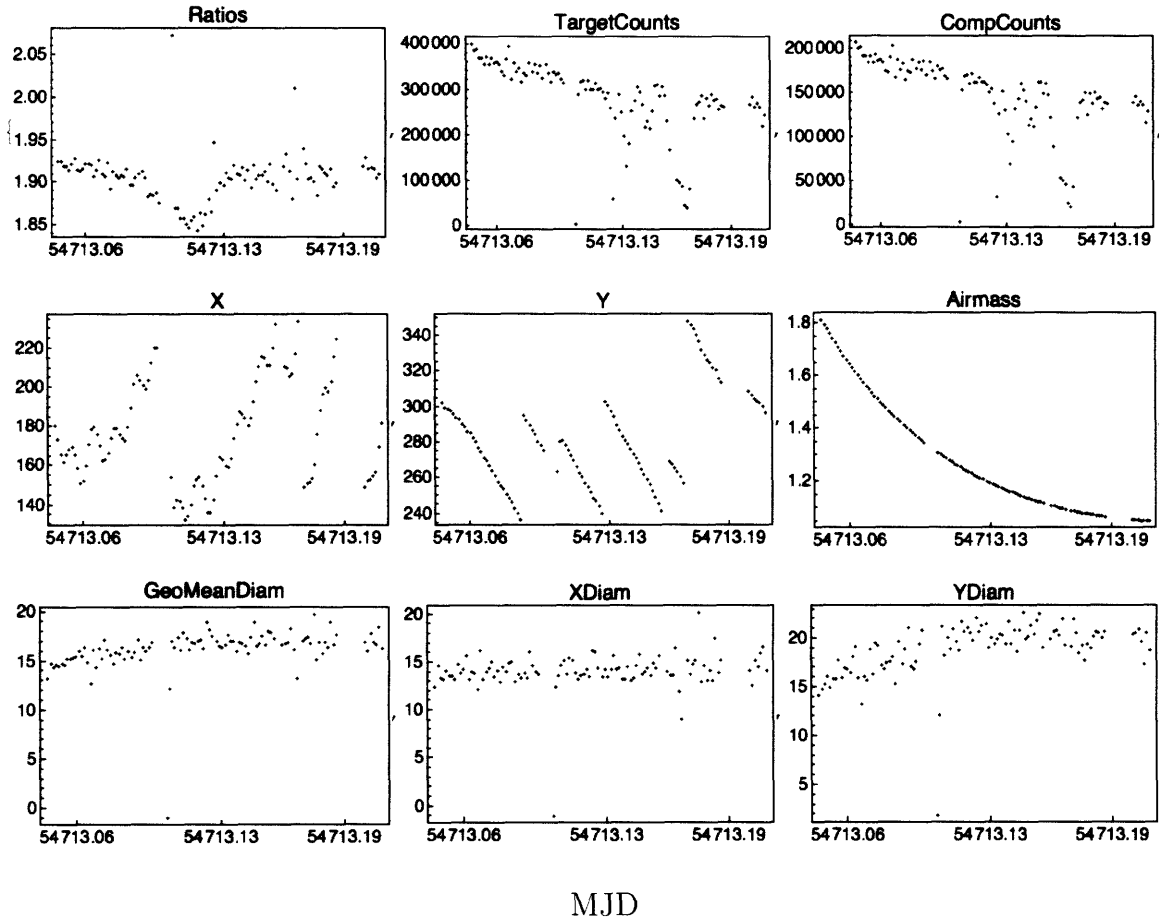
Figure B-19: Interesting quantities from 20080904 (WAO). The two sets of simultaneous dips in the number of target star and comparison star counts are likely the result of clouds drifting through the field of view. The roughly fifteen-minute oscillation in the x position of the target star is caused by periodic error in the telescope mount. The jumps in the y position of the target star are caused by a combination of guiding errors and manual repointings.
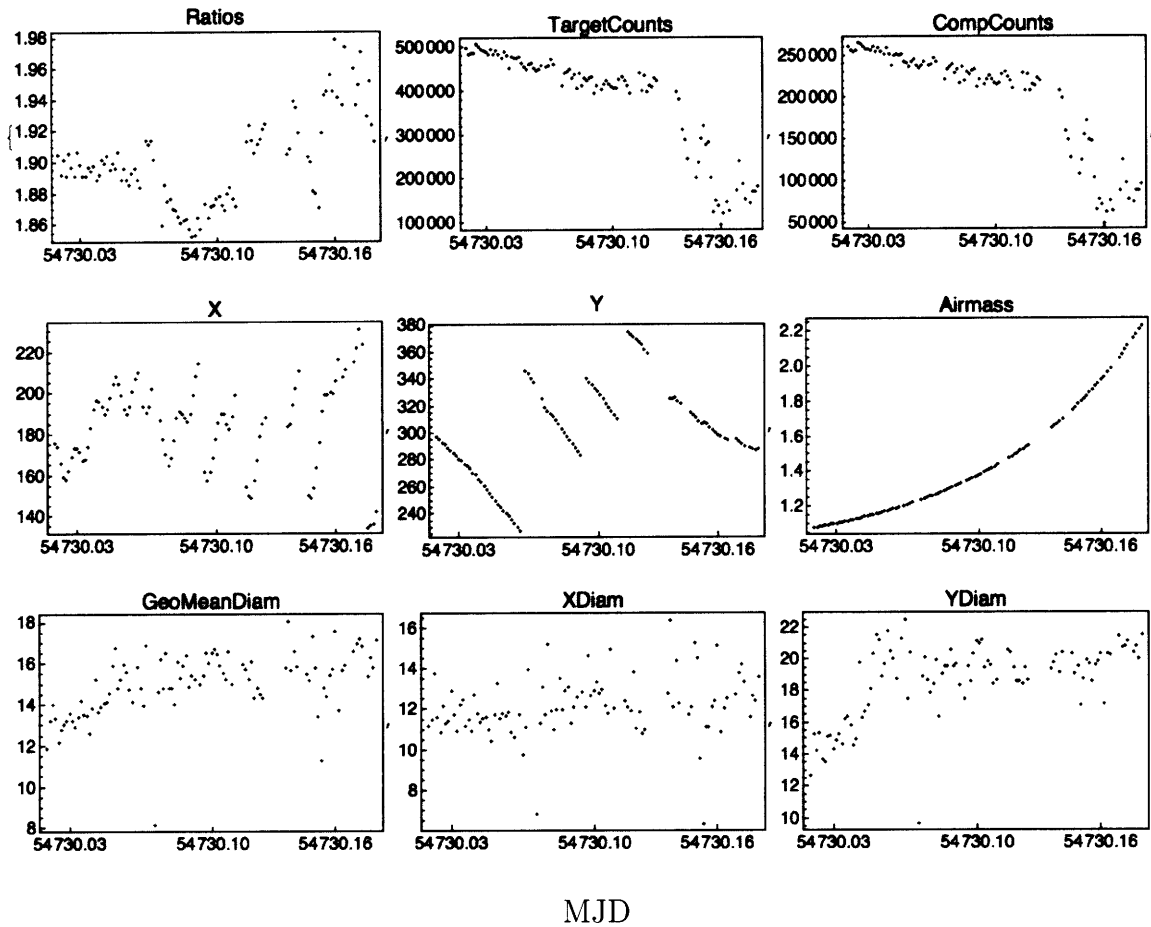
Figure B-20: Interesting quantities from 20080921 (WAO). The roughly fifteen-minute oscillation in the x position of the target star is caused by periodic error in the telescope mount. The jumps in the y position of the target star are caused by a combination of guiding errors and manual repointings.
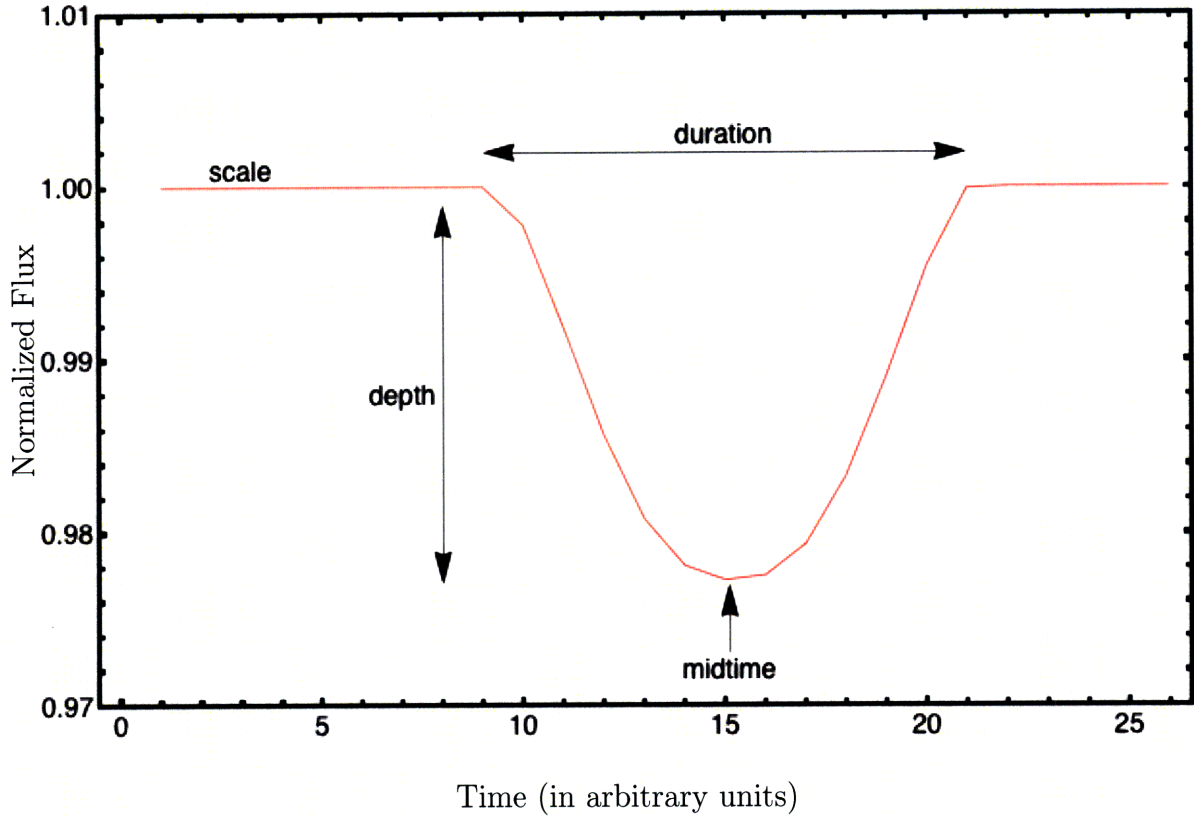
Figure B-21: The features of a hypothetical model light curve for TrES-3 are labeled. *Duration* is the elapsed time between first and fourth contact and is mainly a function of planetary orbital elements. *Depth* is a function of the transit parameters *radius ratio* and *impact parameter*. *Midtime* occurs when the centers of the disks of the transiting planet and host star make their closest approach to one another. *Scale* is the average ratio of the target star to the comparison star in the baseline part of the light curve. In this plot scale is been normalized such that the value of the model light curve is unity during baseline. The overall shape of the light curve, particularly the degree to which the bottom of the light curve is flattened, is strongly affected by the limb-darkening transit parameters u and v. See section 6.2 for a more detailed explanation of transit parameters and their effects on light curve features.
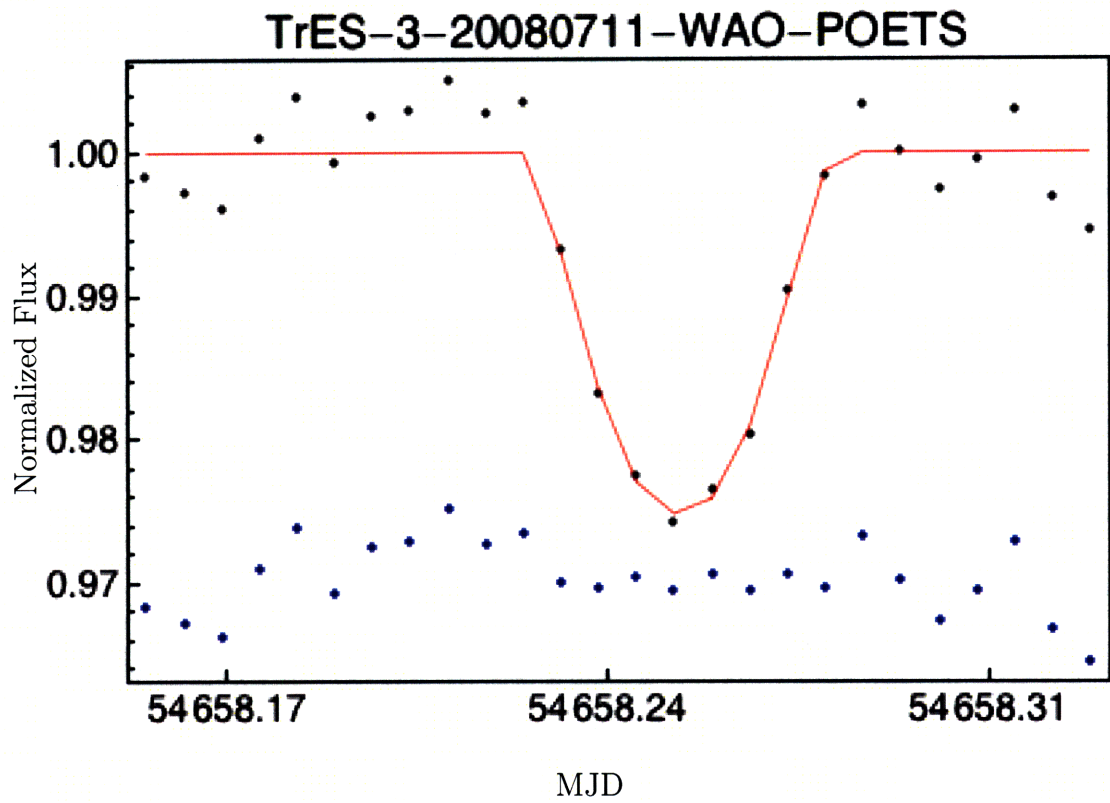
Figure B-22: Binned data from 20080711 are plotted as black points. A model light curve, resulting from an individual (single-night) fit of the parameters duration, radius ratio, impact parameter, scale, and midtime, is plotted as a red line. Residuals are plotted below the light curve as blue points.
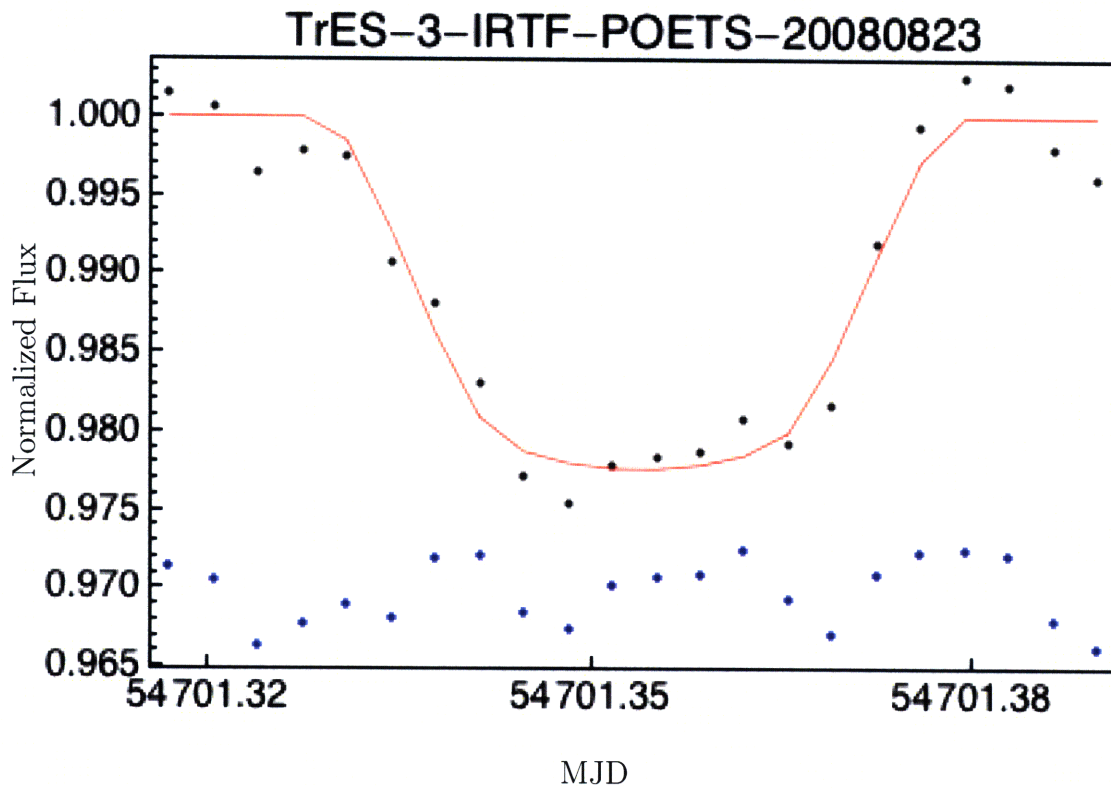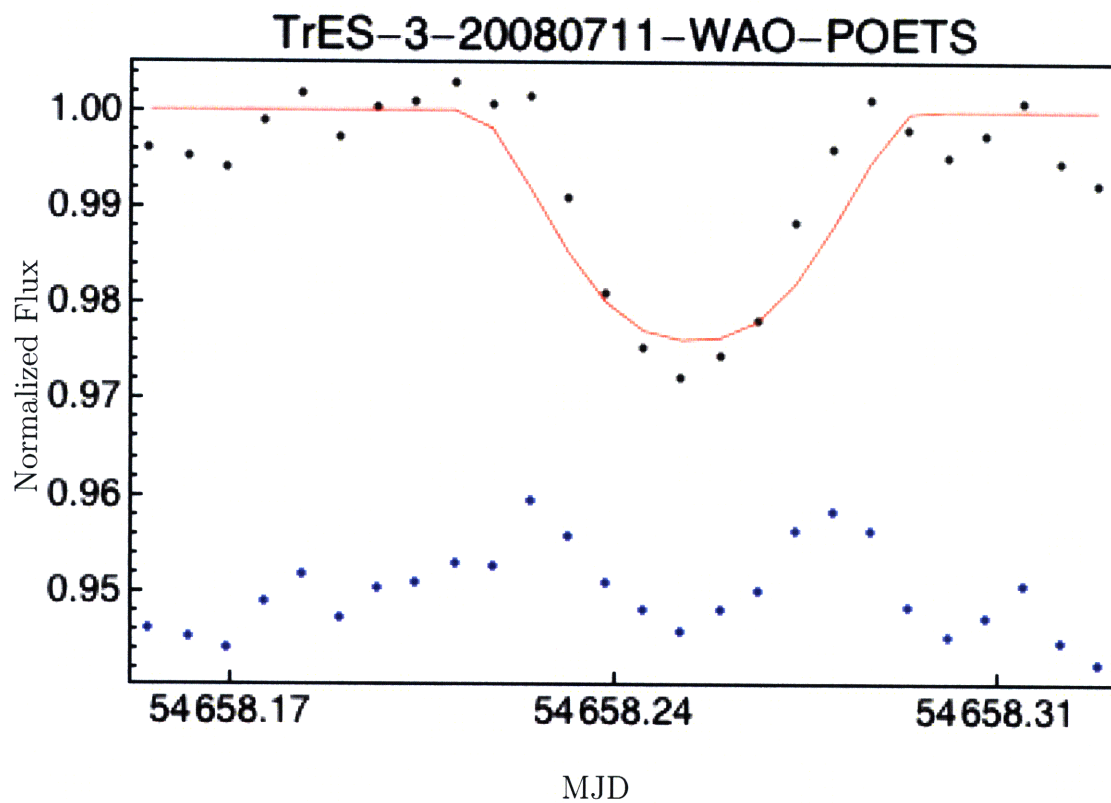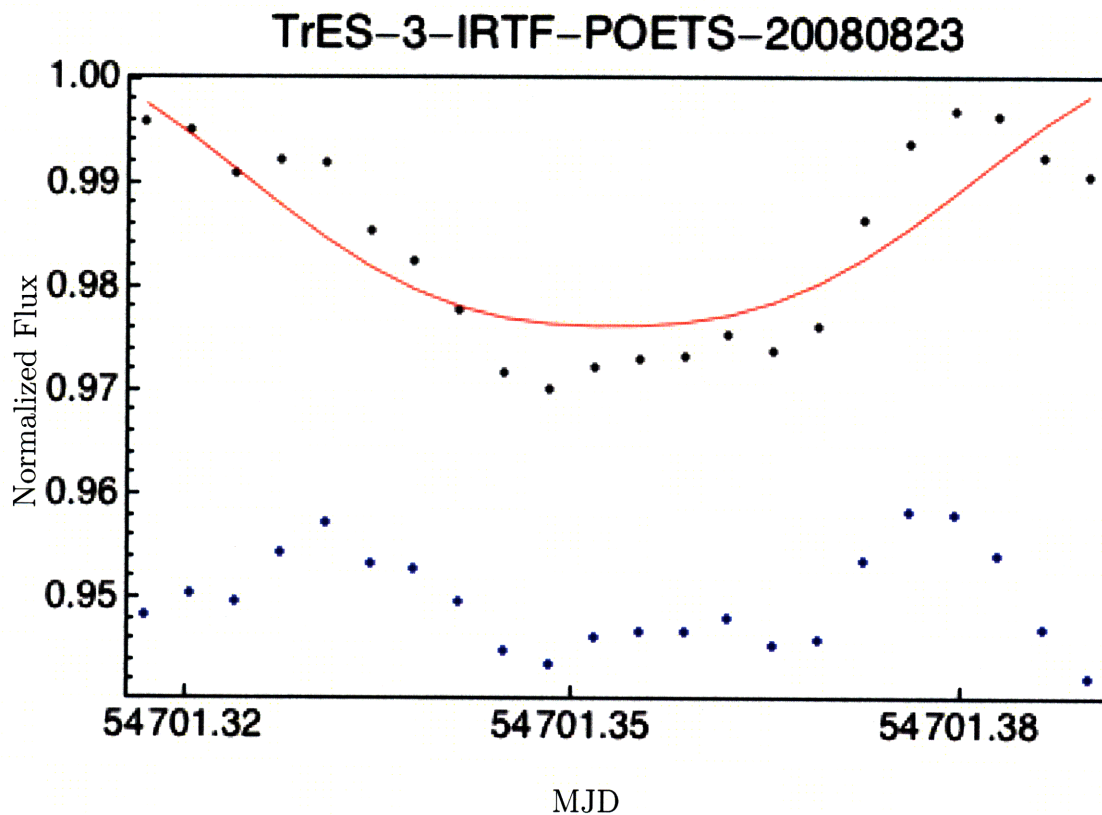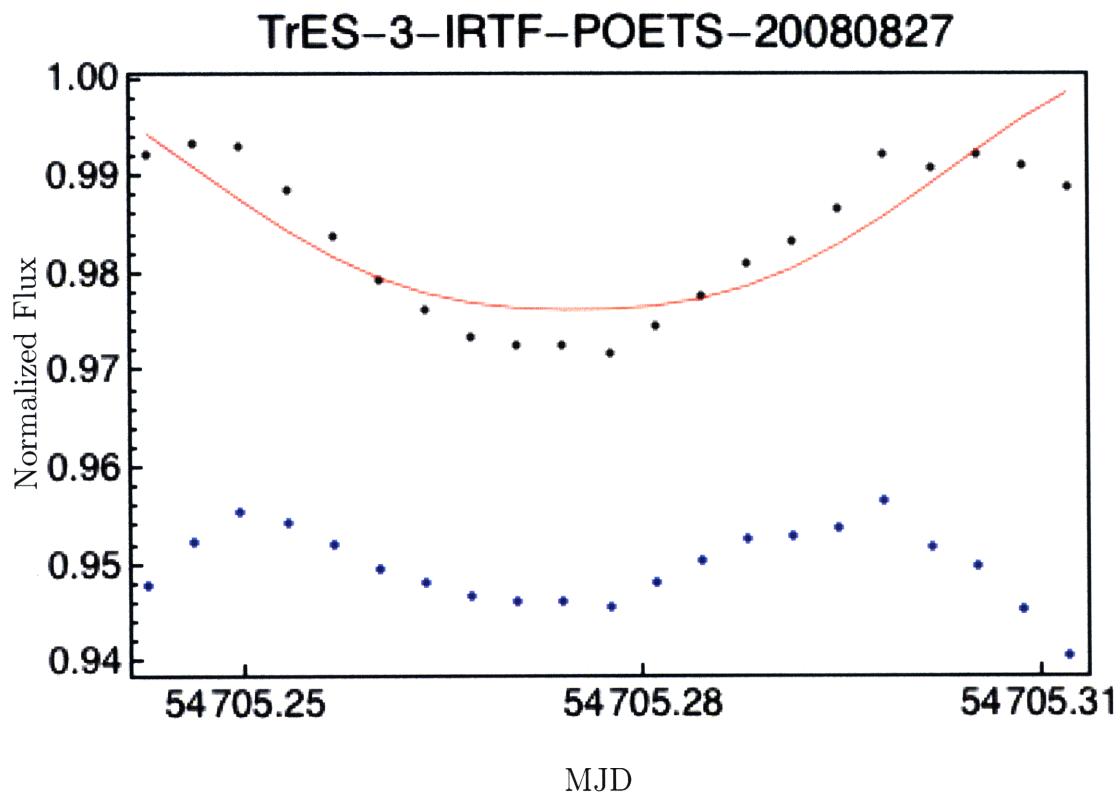
Figure B-23: Binned data from 20080823 are plotted as black points. A model light curve, resulting from an individual (single-night) fit of the parameters duration, radius ratio, impact parameter, scale, and midtime, is plotted as a red line. Residuals are plotted below the light curve as blue points.
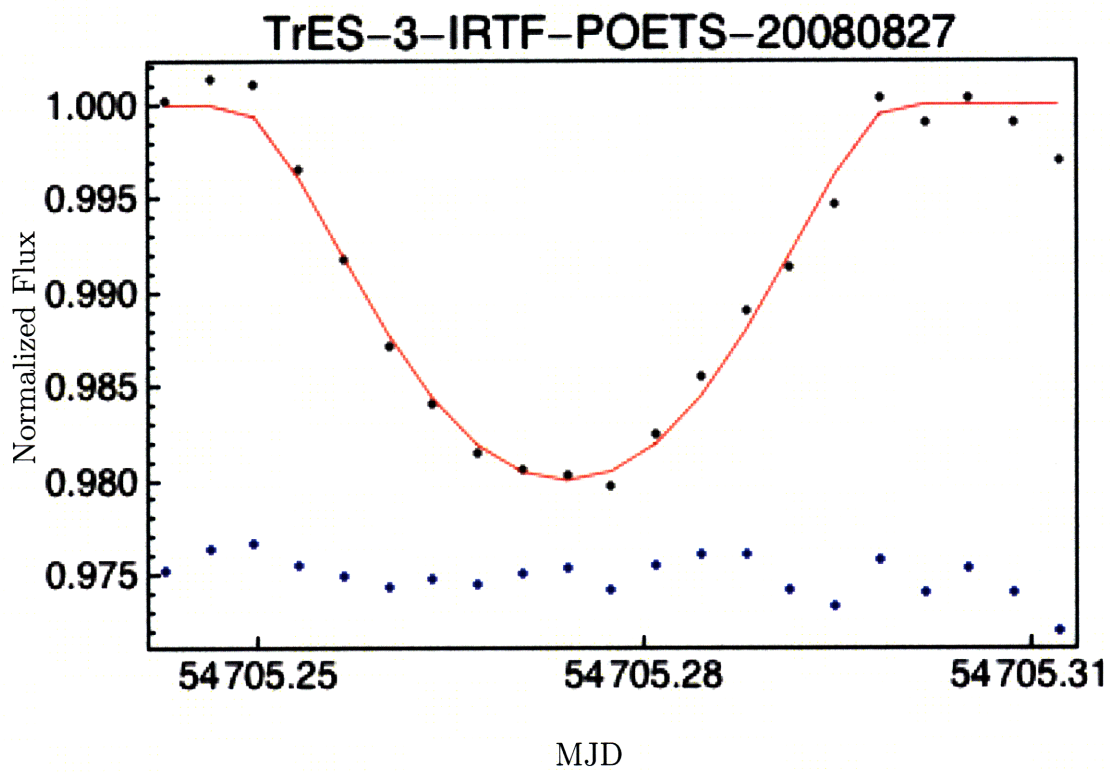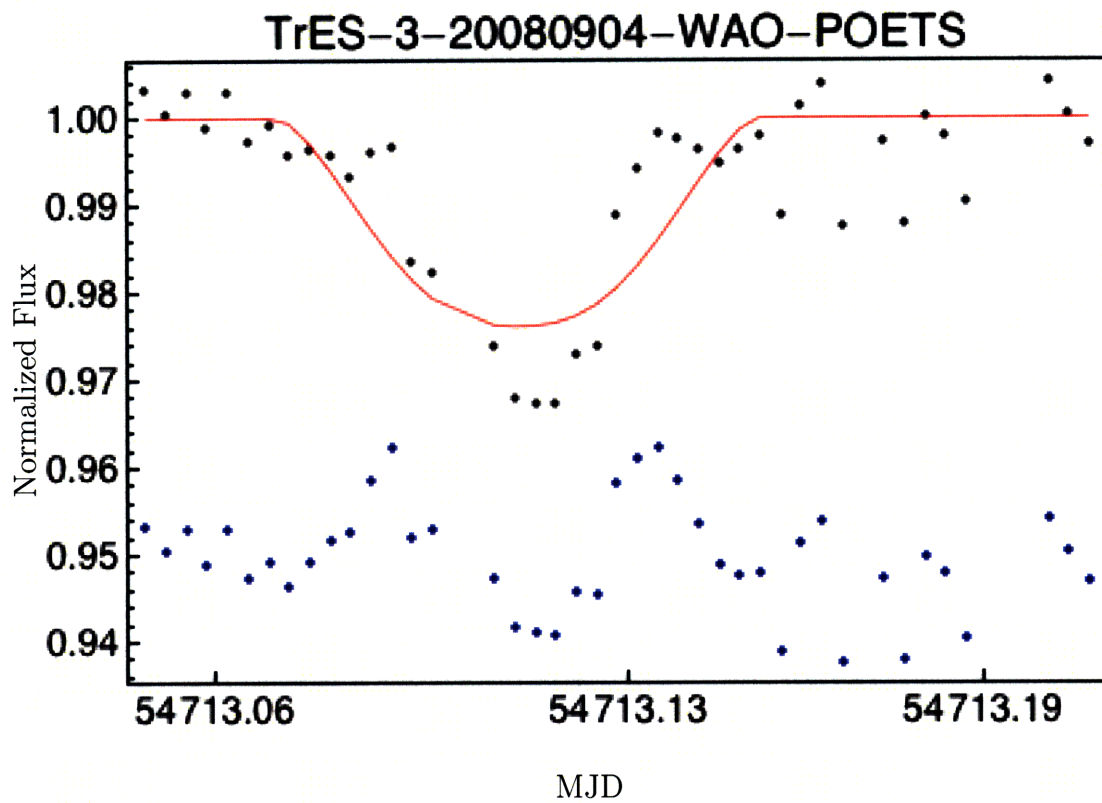
Figure B-24: Binned data from 20080827 are plotted as black points. A model light curve, resulting from an individual (single-night) fit of the parameters duration, radius ratio, impact parameter, scale, and midtime, is plotted as a red line. Residuals are plotted below the light curve as blue points.
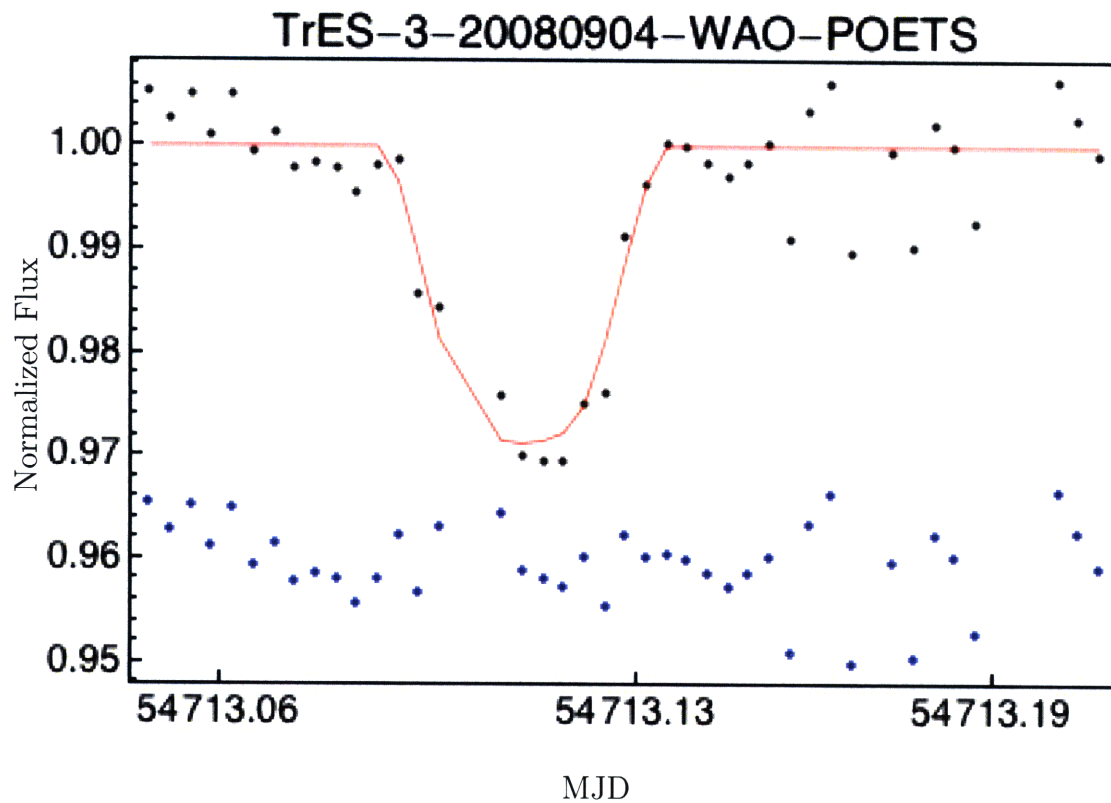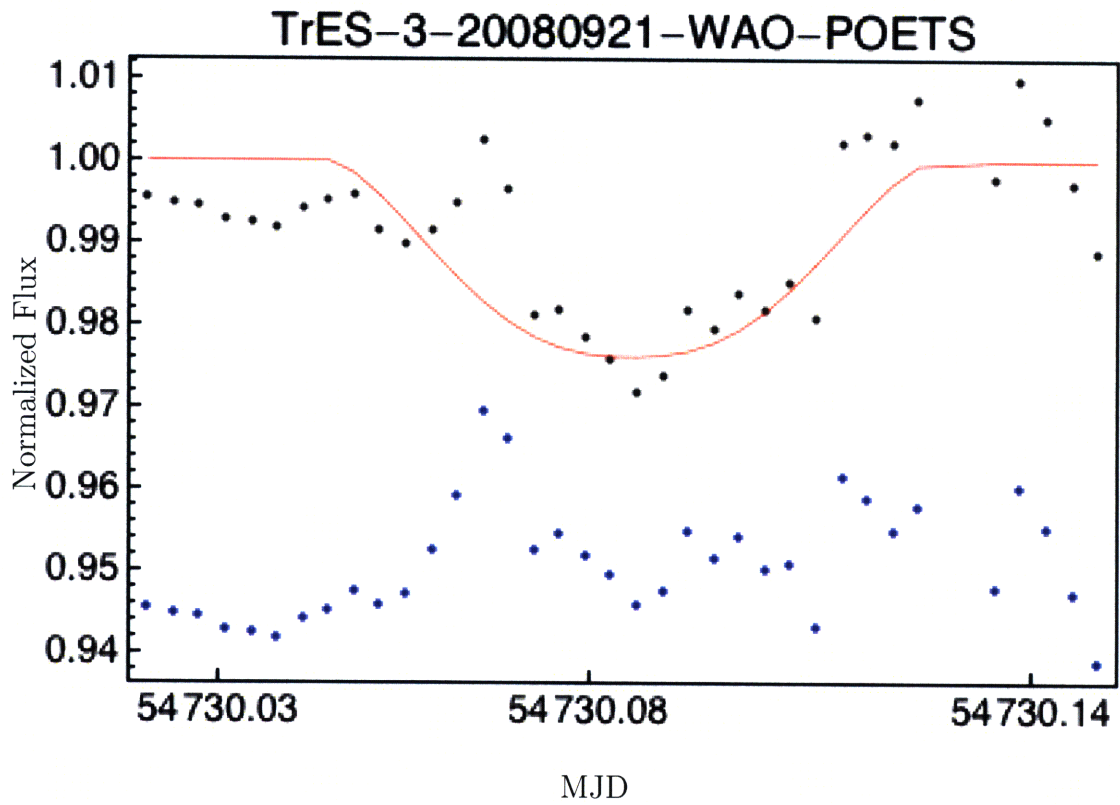
Figure B-25: Binned data from 20080904 are plotted as black points. A model light curve, resulting from an individual (single-night) fit of the parameters duration, radius ratio, impact parameter, scale, and midtime, is plotted as a red line. Residuals are plotted below the light curve as blue points.
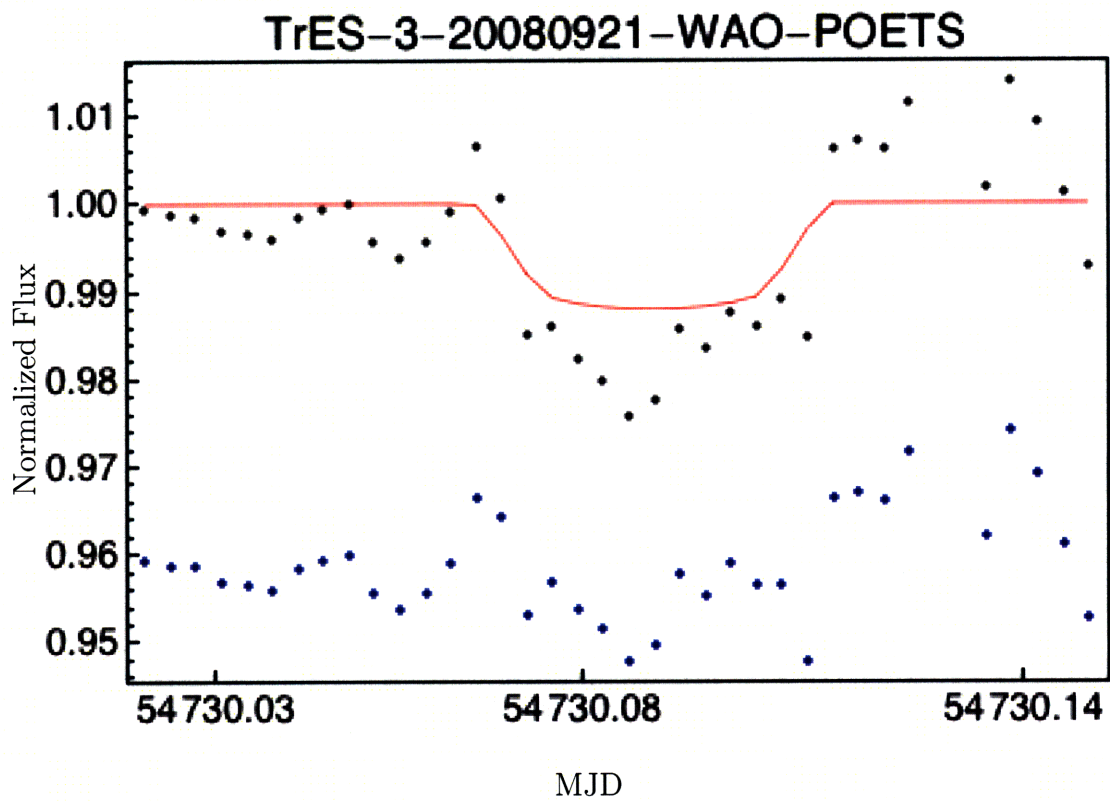
Figure B-26: Binned data from 20080921 are plotted as black points. A model light curve, resulting from an individual (single-night) fit of the parameters duration, radius ratio, impact parameter, scale, and midtime, is plotted as a red line. Residuals are plotted below the light curve as blue points.

Figure B-27: Binned data from 20080711 are plotted as black points. A model light curve, resulting from an individual (single-night) fit of the parameters scale and midtime, is plotted as a red line. Residuals are plotted below the light curve as blue points.
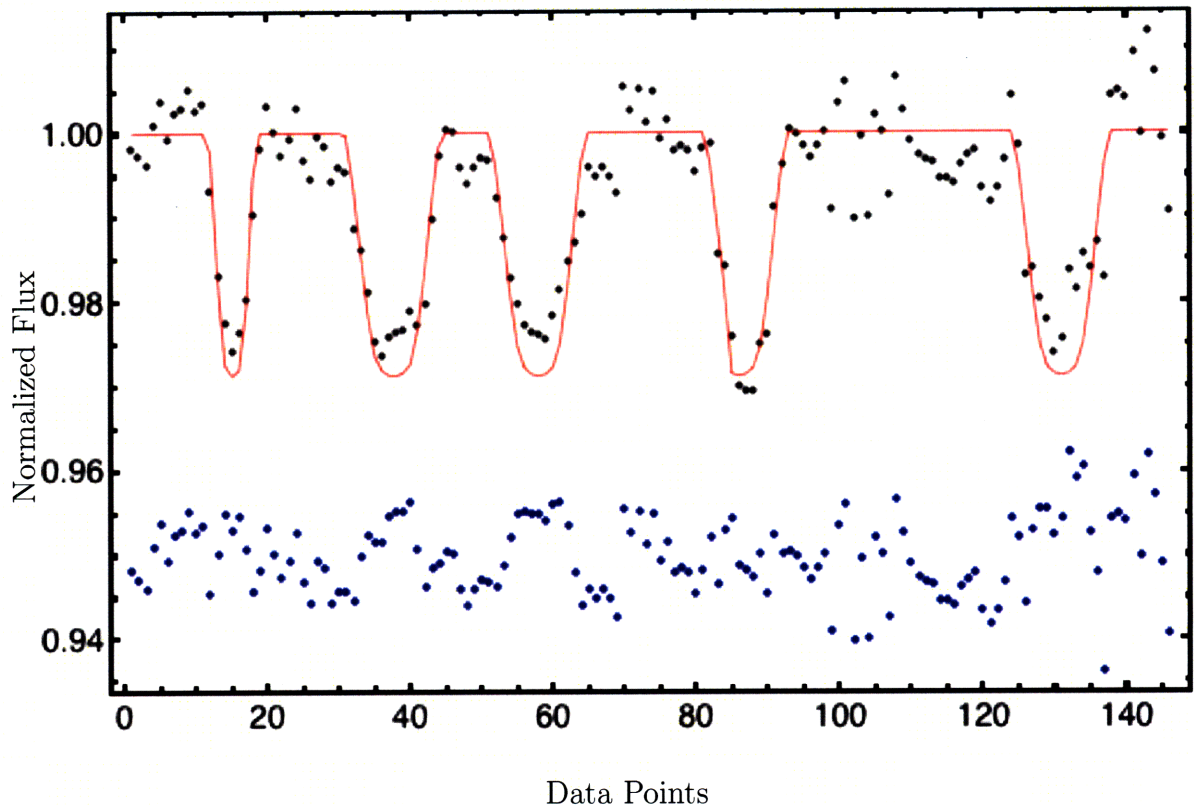
Figure B-28: Binned data from 20080823 are plotted as black points. A model light curve, resulting from an individual (single-night) fit of the parameters scale and mid-time, is plotted as a red line. Residuals are plotted below the light curve as blue points.

Figure B-29: Binned data from 20080827 are plotted as black points. A model light curve, resulting from an individual (single-night) fit of the parameters scale and mid-time, is plotted as a red line. Residuals are plotted below the light curve as blue points.

Figure B-30: Binned data from 20080904 are plotted as black points. A model light curve, resulting from an individual (single-night) fit of the parameters scale and mid-time, is plotted as a red line. Residuals are plotted below the light curve as blue points.

Figure B-31: Binned data from 20080921 are plotted as black points. A model light curve, resulting from an individual (single-night) fit of the parameters scale and mid-time, is plotted as a red line. Residuals are plotted below the light curve as blue points.

Figure B-32: Binned data are plotted as black points. A model light curve, resulting from a joint (five-night) fit of the parameters scale and midtime (ten parameters total), is plotted as a red line. All other parameters were held constant across all five nights of data. Residuals are plotted below the light curve as blue points.
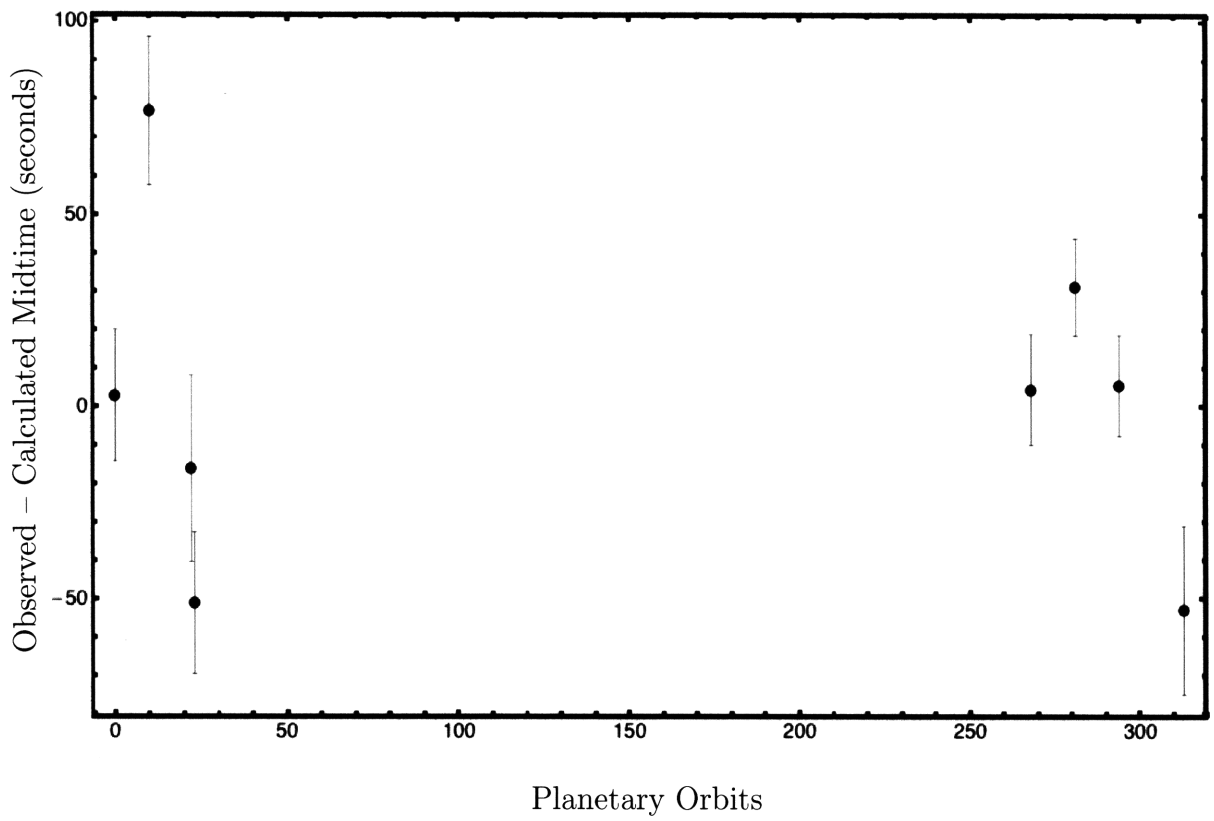
Figure B-33: O-C for events from Sozzetti et al. (2008) [8].
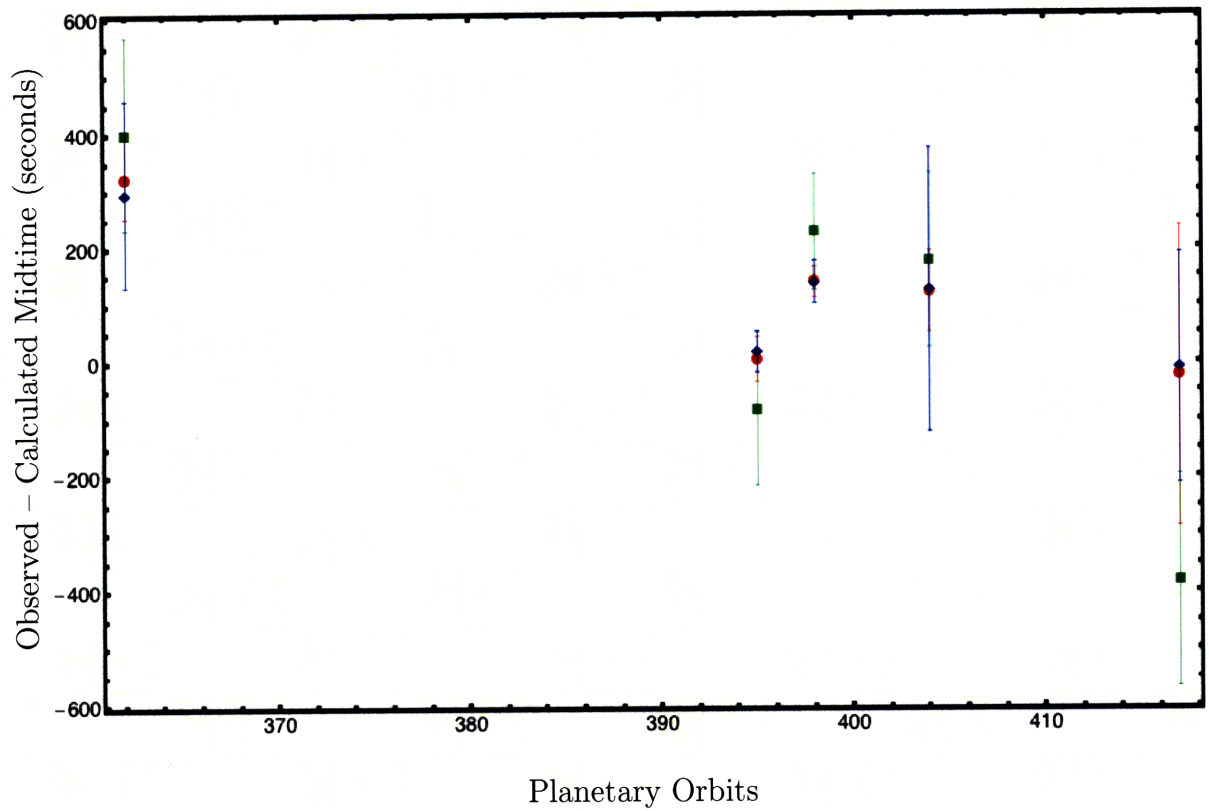
Figure B-34: O-C for various fits. The midtimes of the individual, five-free-parameter fits (set 1) are represented by red circles. The midtimes of the individual, two-free-parameter fits (set 2) are represented by green squares. The midtimes of the joint fit are represented by blue diamonds.
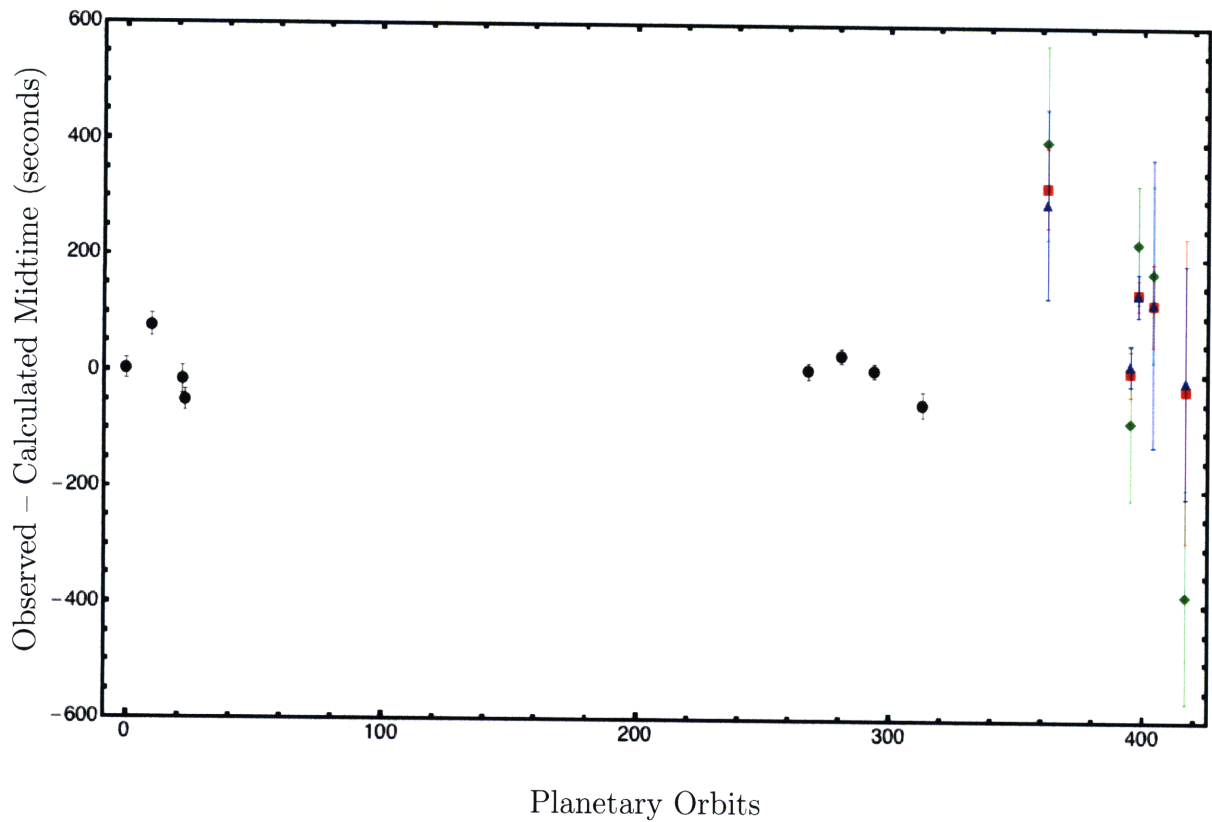
Figure B-35: O-C for various fits. Black circles are events from Sozzetti et al. (2008) [8]. The midtimes of the individual, five-free-parameter fits (set 1) are represented by red squares. The midtimes of the individual, two-free-parameter fits (set 2) are represented by green diamonds. The midtimes of the joint fit are represented by blue triangles.
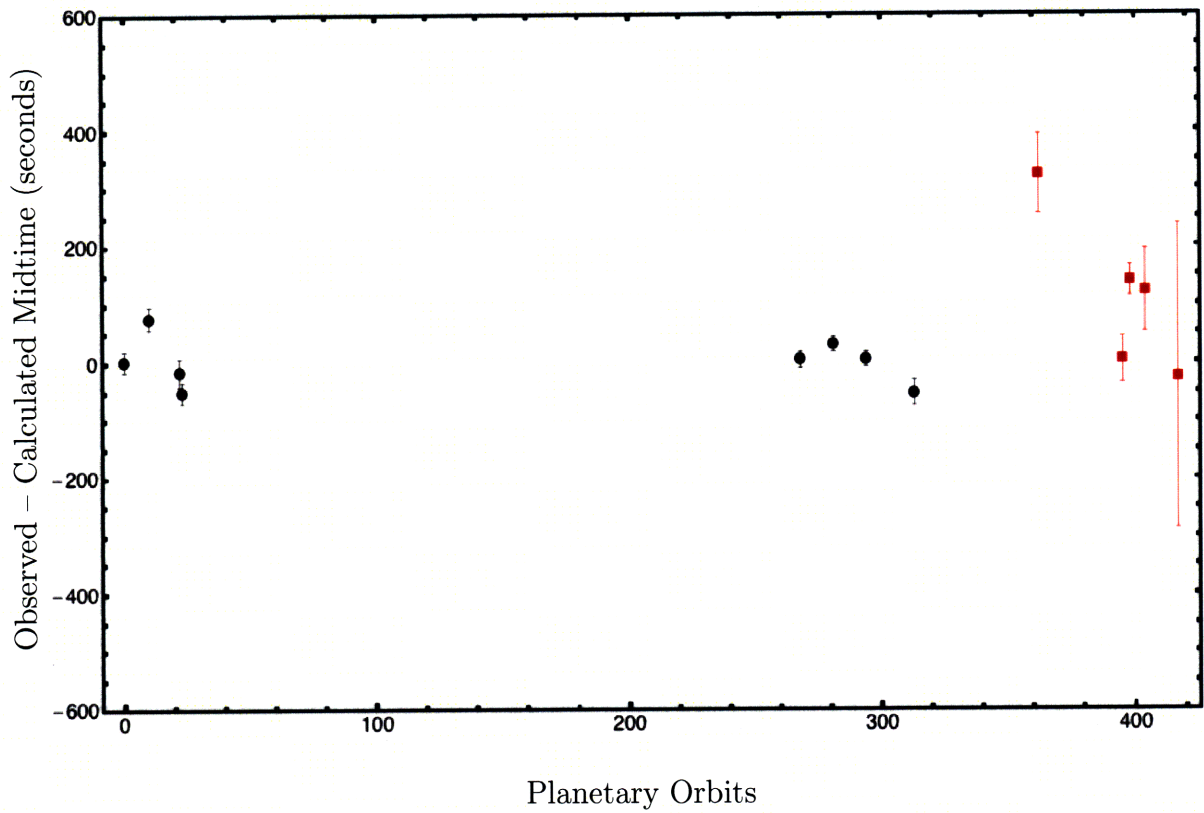
Figure B-36: O-C for individual, five-free-parameter fits. Black circles are events from Sozzetti et al. (2008) [8]. The midtimes of the individual, five-free-parameter fits (set 1) are represented by red squares.
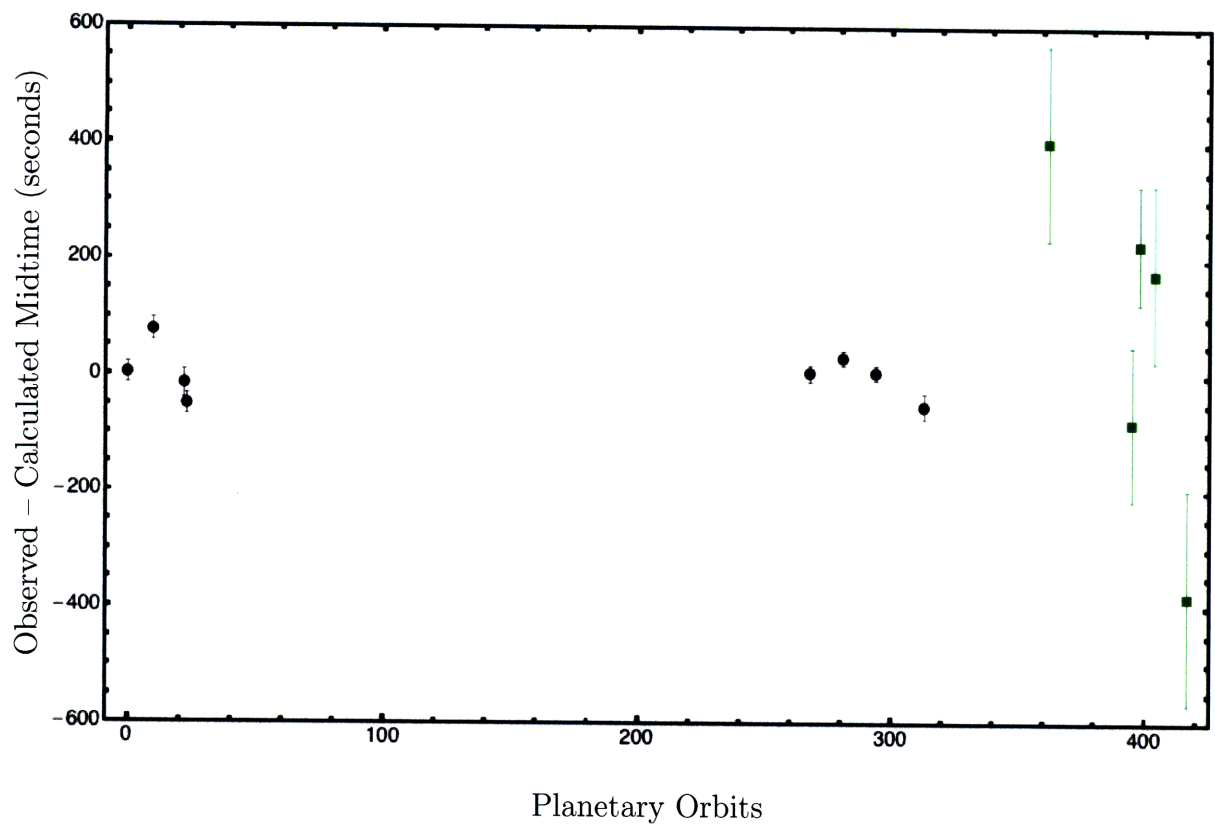
Figure B-37: O-C for individual, two-free-parameter fits. Black circles are events from Sozzetti et al. (2008) [8]. The midtimes of the individual, two-free-parameter fits (set 2) are represented by green squares.
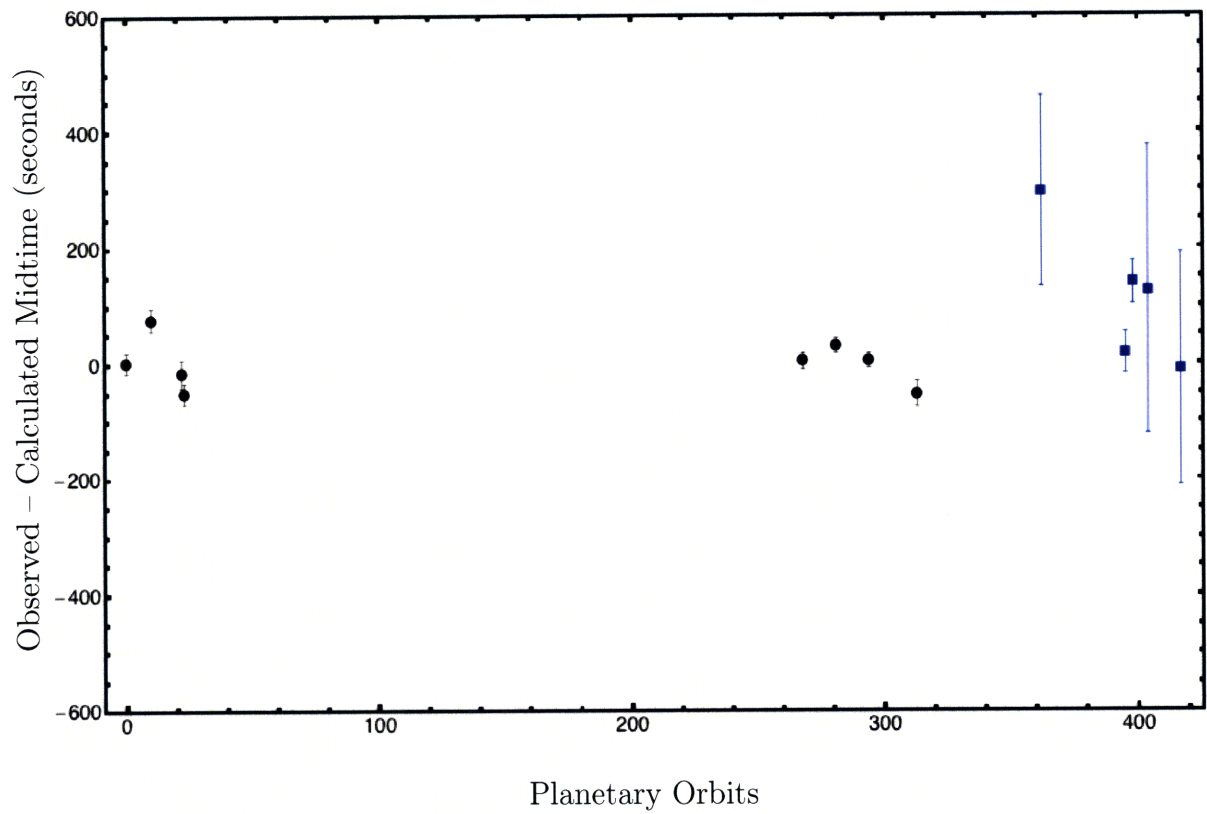
Figure B-38: O-C for joint fit. Black circles are events from Sozzetti et al. (2008) [8]. The midtimes of the joint fit are represented by blue squares.
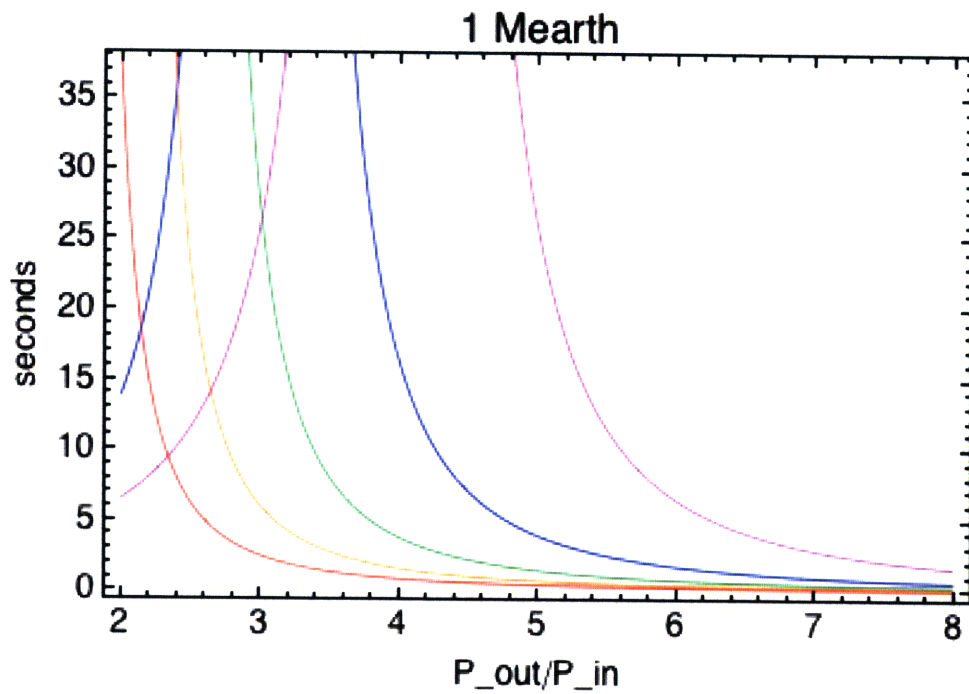
Figure B-39: TTV vs. period ratio at various moderate eccentricities. The five curves (from bottom to top, or red to purple) correspond to eccentricities of 0.1, 0.2, 0.3, 0.4, and 0.5. Generated following the example of Holman & Murray (2005) [4].
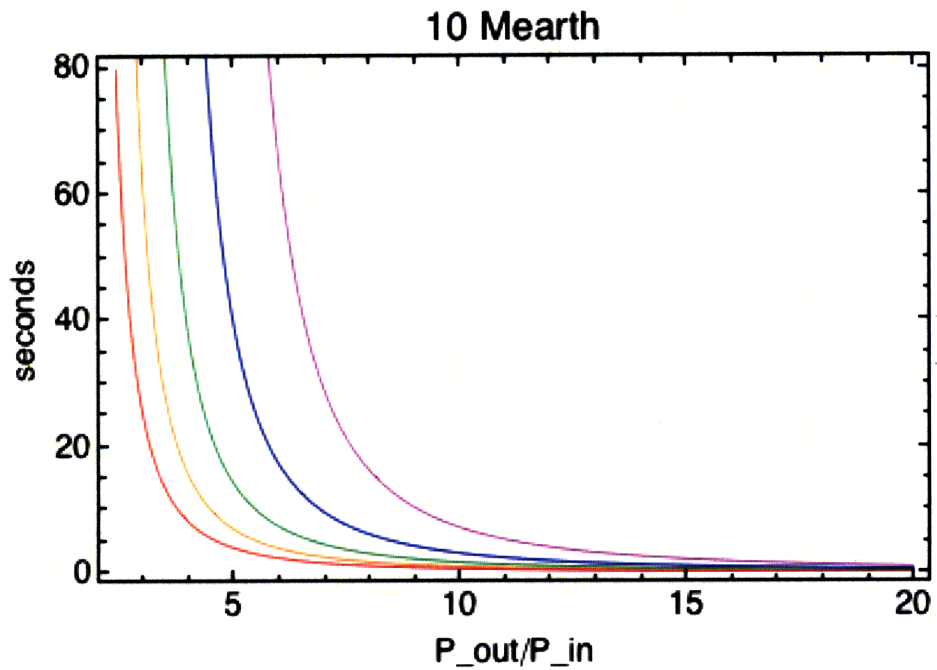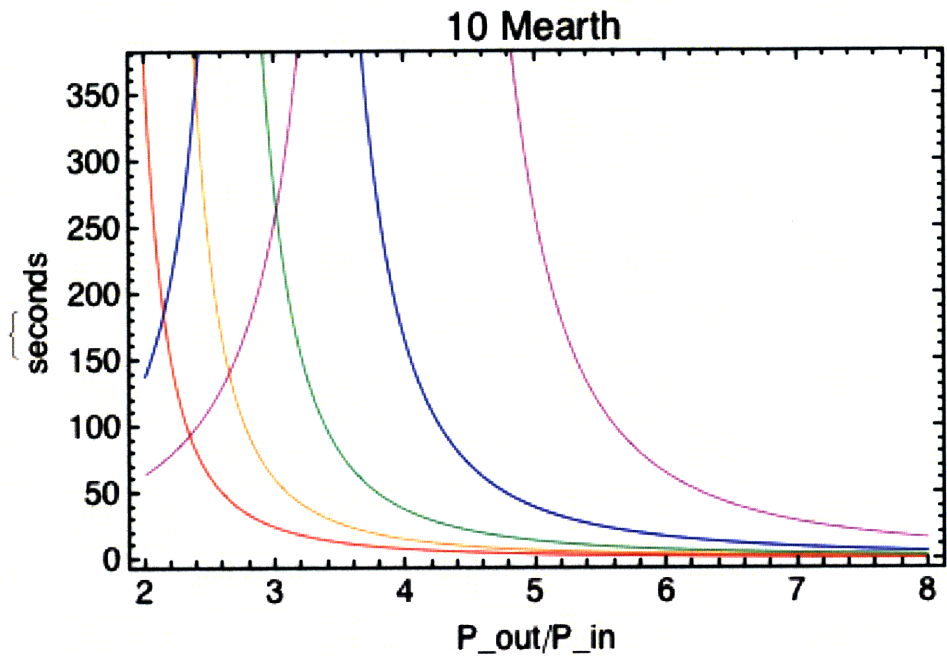
Figure B-40: TTV vs. period ratio at various moderate eccentricities. The five curves in each plot (from bottom to top, or red to purple) correspond to eccentricities of 0.1, 0.2, 0.3, 0.4, and 0.5. The two plots differ only in the range of period ratios plotted. Generated following the example of Holman & Murray (2005) [4].
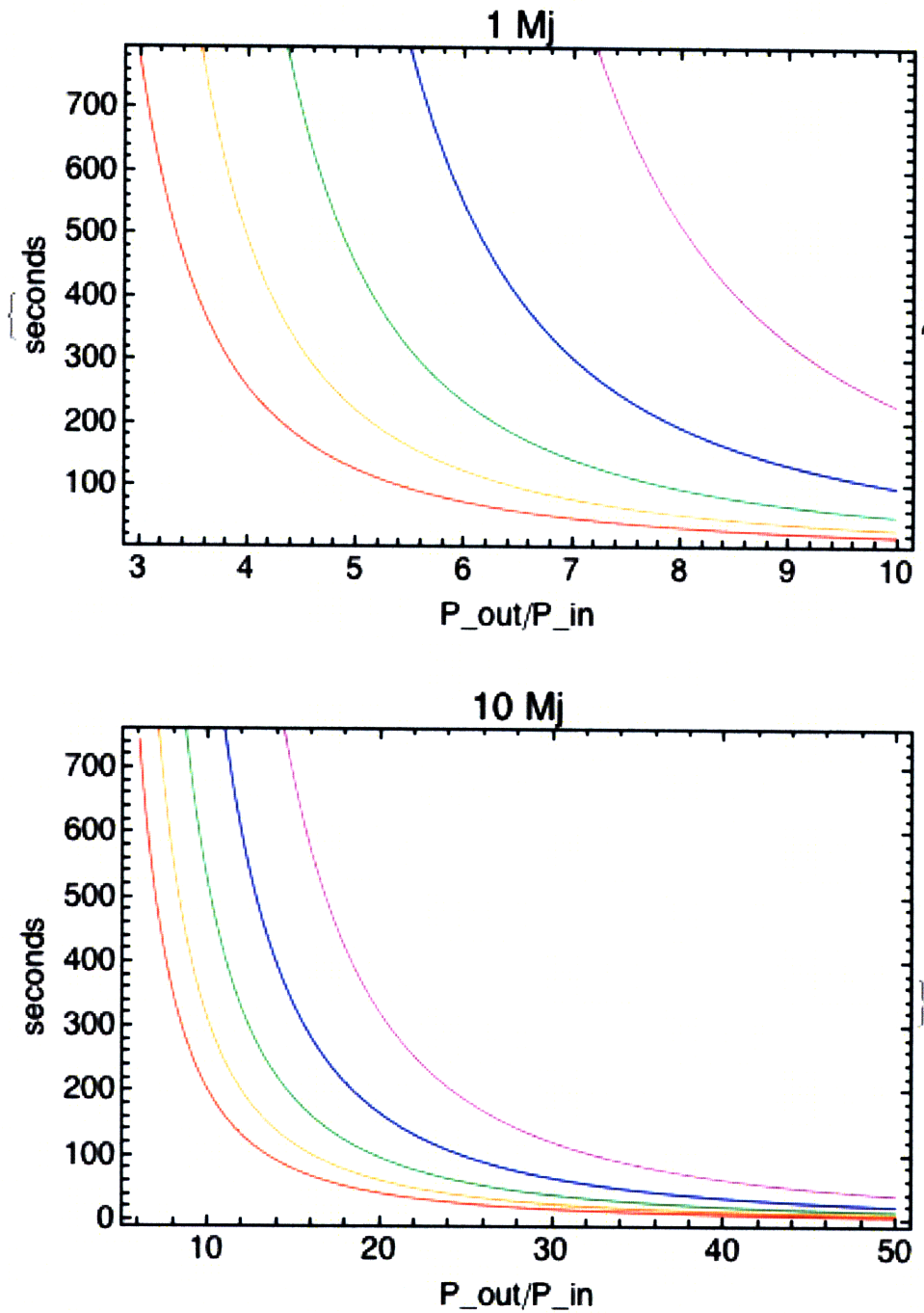
Figure B-41: TTV vs. period ratio at two different perturber masses and various moderate eccentricities. The five curves in each plot (from bottom to top, or red to purple) correspond to eccentricities of 0.1, 0.2, 0.3, 0.4, and 0.5. Generated following the example of Holman & Murray (2005) [4].
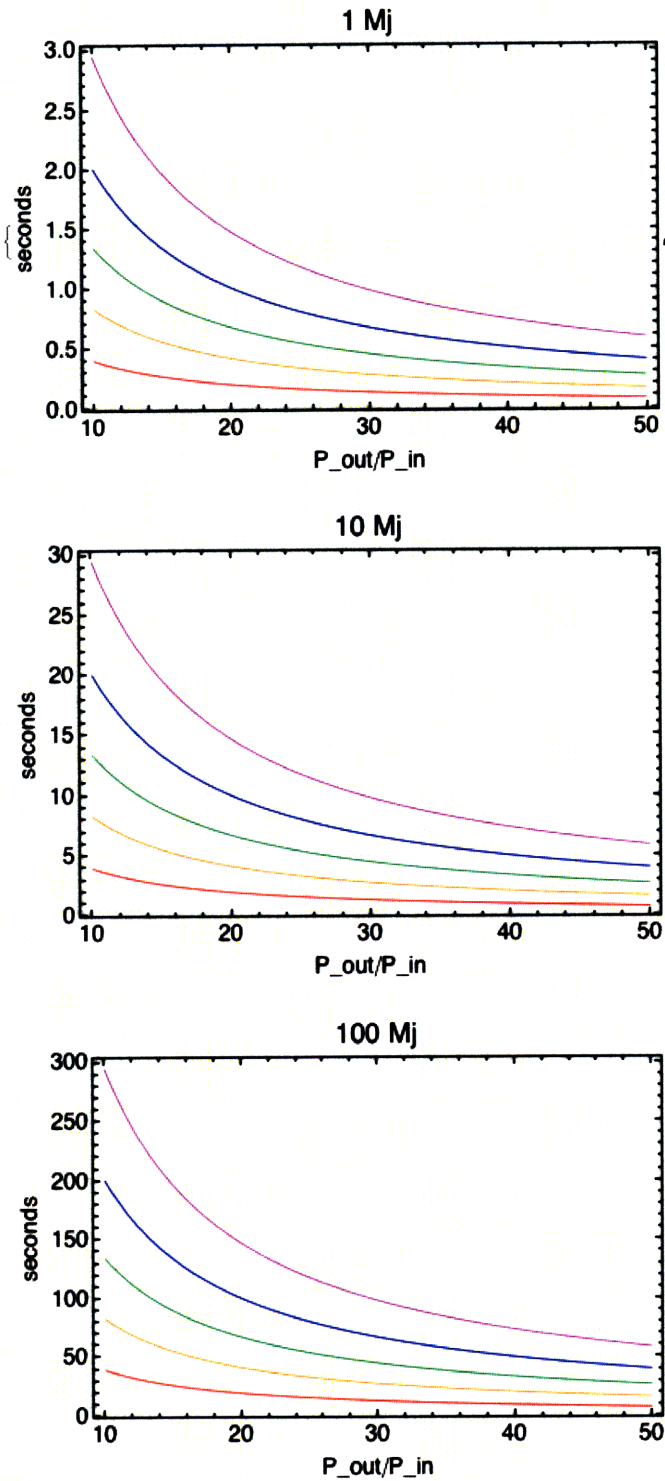
94

Figure B-42: TTV vs. period ratio for three different perturber masses at various moderate eccentricities. The five curves in each plot (from bottom to top, or red to purple) correspond to eccentricities of 0.1, 0.2, 0.3, 0.4, and 0.5. Generated following the example of Agol et al. (2005) [2].
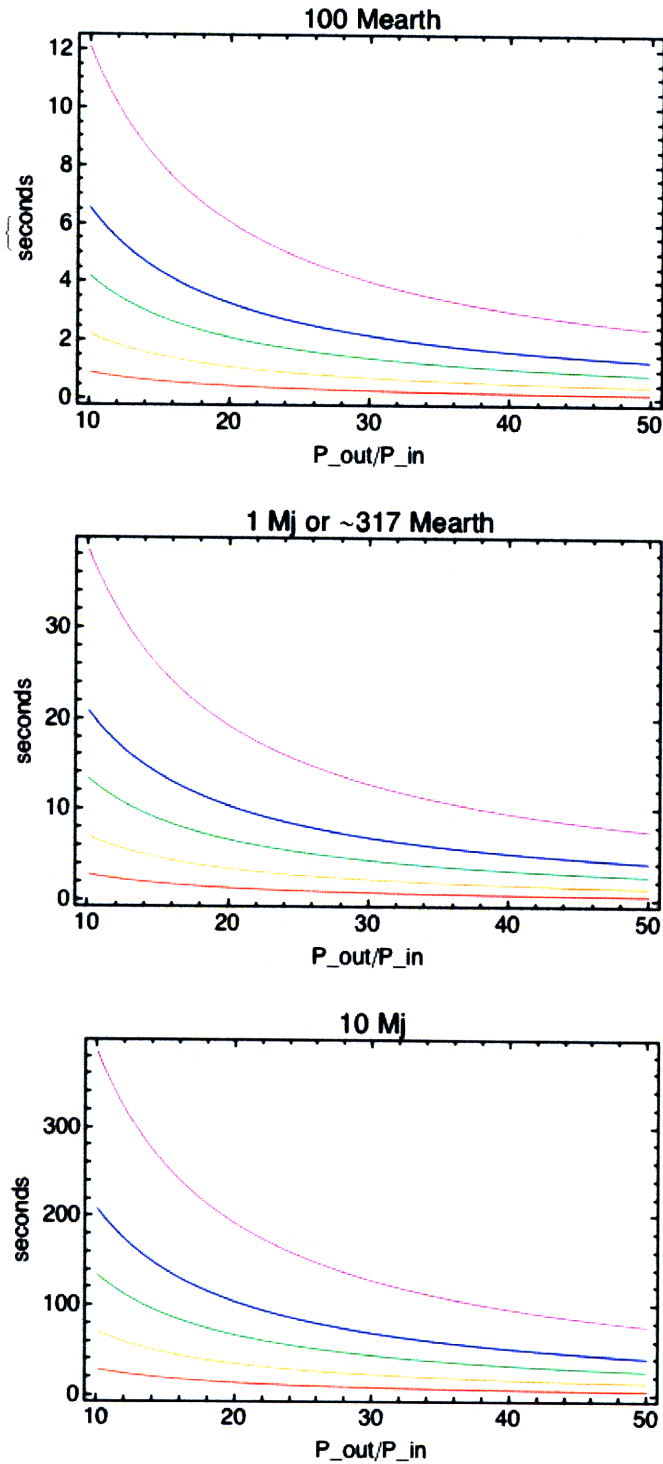
Figure B-43: TTV vs. period ratio for three different perturber masses at various large eccentricities. The five curves in each plot (from bottom to top, or red to purple) correspond to eccentricities of 0.5, 0.7, 0.8, 0.85, and 0.9. Generated following the example of Agol et al. (2005) [2].
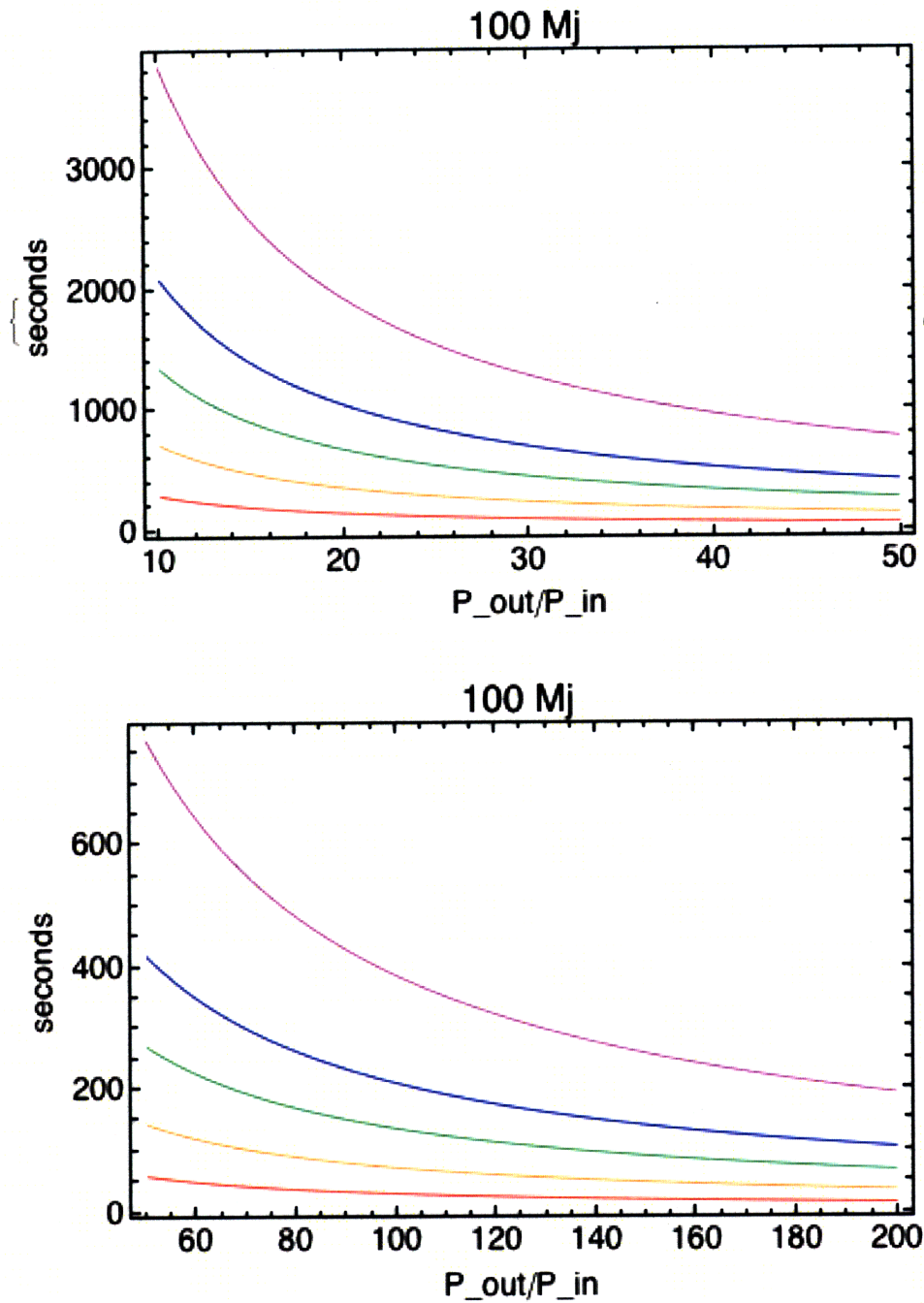
Figure B-44: TTV vs. period ratio for a 100 M_J perturber at various large eccentricities. The five curves in each plot (from bottom to top, or red to purple) correspond to eccentricities of 0.5, 0.7, 0.8, 0.85, and 0.9. The two plots differ only in the range of period ratios plotted. Generated following the example of Agol et al. (2005) [2].
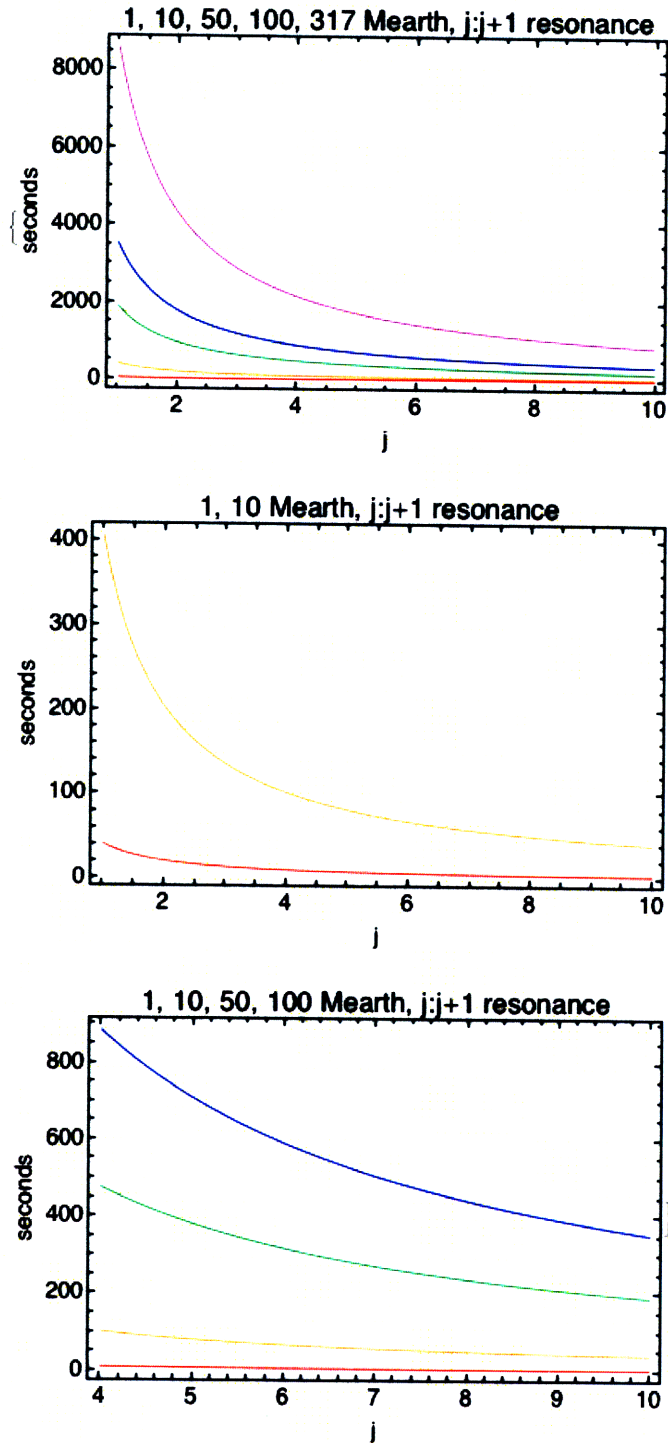
Figure B-45: TTV vs. j for various small perturbers in $j{:}j{+}1$ resonances with TrES-3. The five curves in the top plot (from bottom to top, or red to purple) correspond to masses of 1 M_{Earth}, 10 M_{Earth}, 50 M_{Earth}, 100 M_{Earth}, and 317 M_{Earth} (roughly 1 M_J). The lower and upper curves in the middle plot correspond to masses of 1 M_{Earth} and 10 M_{Earth} respectively. The four curves in the bottom plot (from bottom to top, or red to purple) correspond to masses of 1 M_{Earth}, 10 M_{Earth}, 50 M_{Earth}, and 100 M_{Earth}. The three plots differ only in the range of j and selection of masses plotted. Generated following the example of part 6 of Agol et al. (2005) [2].
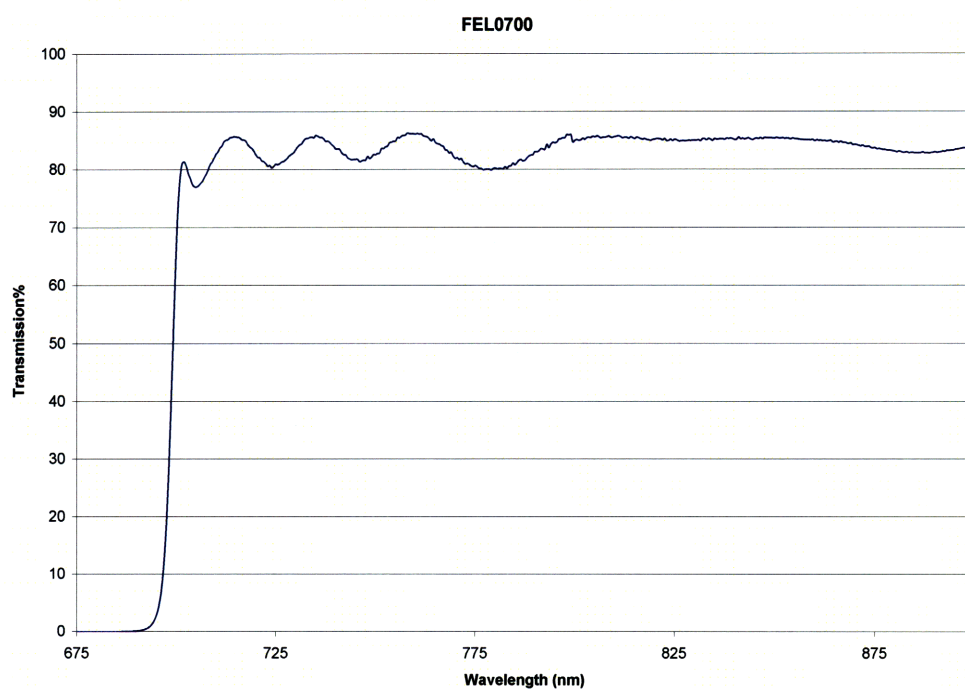
Figure B-46: Transmission spectrum for Thorlabs FEL0700 filter. Image provided by Thorlabs.
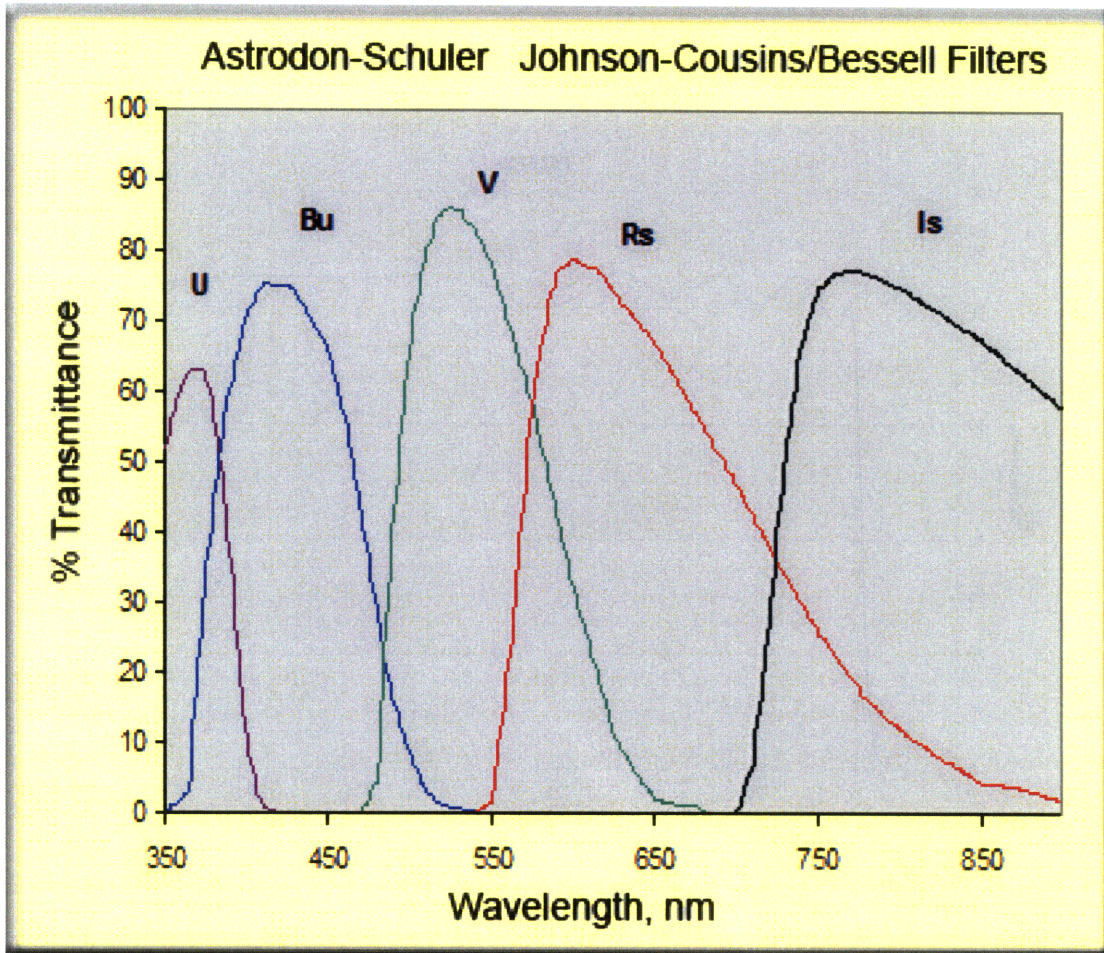
Figure B-47: Transmission spectrum for Schüler / Astrodon Imaging Rs (red) filter. Image provided by Astrodon.
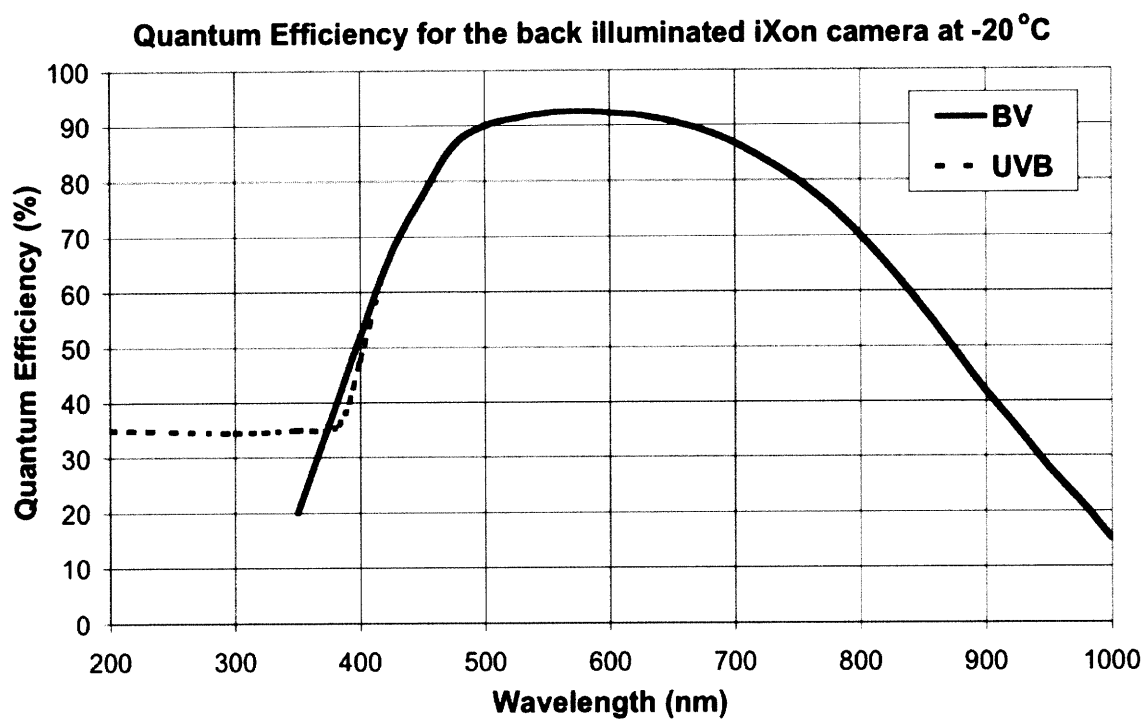
Figure B-48: Quantum efficiency of Andor Ixon DV887 (POETS) detector. Image provided by Andor.

Appendix C

Light Curve Model

The following light curve model (used in the fitting described in section 6) and explanatory text are excerpted directly from Adams [1]:

The drop in flux due to the planetary transit is divided into four cases, based on the distance between the centers of the two bodies. In case (a) the planet is outside the disk of the star; in case (b) the planet partially overlaps but the center is outside the star; in case (c) the planet partially overlaps and the center is inside the star; and in case (d) the planet completely overlaps the disk of the star. The transit light curve is calculated for each point using:

$$F = 1 - \Delta_F / F_{surface},$$
(C.1)

where $F_{surface}$ is the total surface brightness of the star:

$$F_{surface} = 2\pi \int_0^1 r\lambda(r, u, v)dr.$$
(C.2)

The equations for the flux drop ΔF for each case, where D is the separation between the center of the planet and the star, ρ is the radius ratio of the planet to the star, and θ and r' are integration variables, are thus:

$$\Delta F_a = 0,$$
(C.3)

$$\Delta F_b = \int_{-\theta_0}^{\theta_0} \int_{r'_{min}}^{\rho} D\lambda(\sqrt{D^2 + r'^2 - 2Dr'cos\theta}, u, v) d\theta dr', \qquad (C.4)$$

$$\Delta F_c = \int_0^{2\pi} \int_0^{r'_{max}} D\lambda(\sqrt{D^2 + r'^2 - 2Dr'cos\theta}, u, v) d\theta dr', \qquad (C.5)$$

$$\Delta F_d = \int_0^{2\pi} \int_0^{\rho} D\lambda(\sqrt{D^2 + r'^2 - 2Dr'cos\theta}, u, v) d\theta dr'. \qquad (C.6)$$

The limb darkening at a distance r from the center of the star has the form

$$\lambda(r, u, v) = 1 - u(1 - \mu) - v(1 - \mu^2) \qquad (C.7)$$

where

$$\mu = \sqrt{1 - r^2}. \qquad (C.8)$$

The limits of integration are geometrically derived and can be calculated using the equations

$$\theta_0 = Arccos\left(\frac{r^2 + \rho^2 - 1}{2r\rho}\right), \qquad (C.9)$$

$$r'_{min} = 2rcos\theta - \frac{1}{2}\sqrt{(2rcos\theta)^2 - 4(r^2 - 1)}, \qquad (C.10)$$

$$r'_{max} = \begin{cases} 0 & \text{if } 0 < \theta \leq \theta_0 \\ & \text{or } 2\pi - \theta_0 < \theta < 2\pi \\ \\ 2rcos\theta + \frac{1}{2}\sqrt{(2rcos\theta)^2 - 4(r^2 - 1)} & \text{otherwise} \end{cases} \qquad (C.11)$$

References

[1] E. R. Adams. *Transit Timing with Fast Cameras on Large Telescopes*. PhD thesis, Massachusetts Institute of Technology, in preparation.

[2] E. Agol, J. Steffen, R. Sari, and W. Clarkson. On detecting terrestrial planets with timing of giant planet transits. MNRAS, 359:567–579, May 2005.

[3] F. Bonnarel, P. Fernique, O. Bienaymé, D. Egret, F. Genova, M. Louys, F. Ochsenbein, M. Wenger, and J. G. Bartlett. The ALADIN interactive sky atlas. A reference tool for identification of astronomical sources. A&AS, 143:33–40, April 2000.

[4] M. J. Holman and N. W. Murray. The Use of Transit Timing to Detect Terrestrial-Mass Extrasolar Planets. *Science*, 307:1288–1291, February 2005.

[5] F. T. O'Donovan, D. Charbonneau, G. Á. Bakos, G. Mandushev, E. W. Dunham, T. M. Brown, D. W. Latham, G. Torres, A. Sozzetti, G. Kovács, M. E. Everett, N. Baliber, M. G. Hidas, G. A. Esquerdo, M. Rabus, H. J. Deeg, J. A. Belmonte, L. A. Hillenbrand, and R. P. Stefanik. TrES-3: A Nearby, Massive, Transiting Hot Jupiter in a 31 Hour Orbit. ApJ, 663:L37–L40, July 2007.

[6] J. T. Rayner, D. W. Toomey, P. M. Onaka, A. J. Denault, W. E. Stahlberger, W. D. Vacca, M. C. Cushing, and S. Wang. SpeX: A Medium-Resolution 0.8-5.5 Micron Spectrograph and Imager for the NASA Infrared Telescope Facility. PASP, 115:362–382, March 2003.

[7] S. P. Souza, B. A. Babcock, J. M. Pasachoff, A. A. S. Gulbis, J. L. Elliot, M. J. Person, and J. W. Gangestad. POETS: Portable Occultation, Eclipse, and Transit System. PASP, 118:1550–1557, November 2006.

[8] A. Sozzetti, G. Torres, D. Charbonneau, J. N. Winn, S. G. Korzennik, M. J. Holman, D. W. Latham, J. B. Laird, J. Fernandez, F. T. O'Donovan, G. Mandushev, E. Dunham, M. E. Everett, G. A. Esquerdo, M. Rabus, J. A. Belmonte, H. J. Deeg, T. N. Brown, M. G. Hidas, and N. Baliber. A New Spectroscopic and Photometric Analysis of the Transiting Planet Systems TrES-3 and TrES-4. *ArXiv e-prints*, September 2008.

[9] J. H. Steffen and E. Agol. An analysis of the transit times of TrES-1b. MNRAS, 364:L96–L100, November 2005.

[10] D. Veras and E. B. Ford. Identifying Non-transiting Terrestrial Planets with Transit Timing Data. In *IAU Symposium*, volume 253 of *IAU Symposium*, pages 486–489, February 2009.